

Structure and Stability of Charge-Coupled Lanthanide-Substituted $\text{Ca}_{10}(\text{PO}_4)_6\text{F}_2$ as a Potential Fluoride Bearing Nuclear Waste Form

Pratik Das,* Bal Govind Vats,* Pradeep Samui, Abhishek Kumar Rai, Ashok Kumar Yadav, Muhammed Shafeeq, Swayam Kesari, and Suresh Chandra Parida*



Cite This: *ACS Omega* 2024, 9, 35873–35887



Read Online

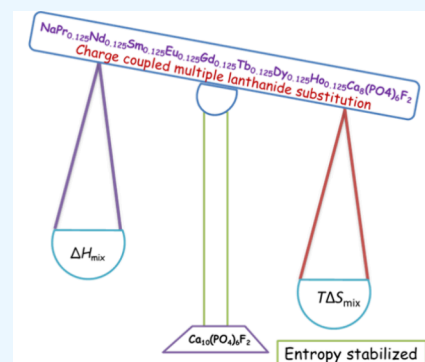
ACCESS |

Metrics & More

Article Recommendations

Supporting Information

ABSTRACT: The structure and stability of charge-coupled lanthanide-substituted $\text{Ca}_{10}(\text{PO}_4)_6\text{F}_2$ as a potential fluoride-bearing nuclear waste form for the back-end fuel cycle of Gen-IV molten salt reactor have been studied in detail. Here, calcium fluorapatite (CaFAP) as a model structure was taken for incorporation of trivalent lanthanides (Lns, La–Lu except Pm) in a charge-coupled fashion, i.e., $2\text{Ca}^{2+} = \text{Na}^+ + \text{Ln}^{3+}$. In these fluorapatite phases, Na^+ is substituted exclusively at nine coordinated sites, Ca1, while Ln^{3+} is preferentially substituted at seven coordinated sites, Ca2. These compositions are further characterized for the local structure by Fourier transform infrared (FTIR) and Raman spectroscopy. Thermal expansion was measured by high-temperature X-ray diffraction (XRD) and the instantaneous thermal expansion coefficient correlates well with the unsubstituted CaFAP. The heat capacities of these solids were measured by differential scanning calorimetry and drop calorimetry, whereas enthalpies of formation were obtained by high-temperature oxide melt solution calorimetry. The thermodynamic analysis demonstrated that lanthanides having ionic radii closure to Ca^{2+} (Sm^{3+} and Gd^{3+}) imparted higher thermodynamic stability to the substituted CaFAP as compared to that of other Ln^{3+} . According to structural and thermodynamic investigations, entropy-stabilized fluorapatite waste from $\text{NaPr}_{0.125}\text{Nd}_{0.125}\text{Sm}_{0.125}\text{Eu}_{0.125}\text{Gd}_{0.125}\text{Tb}_{0.125}\text{Dy}_{0.125}\text{Ho}_{0.125}\text{Ca}_8(\text{PO}_4)_6\text{F}_2$ (WF-Ln) was successfully synthesized for the first time. Furthermore, electron beam irradiation studies probed by XRD, FTIR, Raman, and X-ray absorption (XAS) spectroscopy implied the radiation resistance nature of this substituted CaFAPs up to 20 MGy.

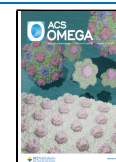


INTRODUCTION

Molten salt reactors (MSRs), a Generation IV reactor concept, are currently one of the most promising options considered for the Th–U fuel cycle.^{1–6} Research on fuel cycle development for MSR is being pursued worldwide. In the Indian nuclear power program, MSR will play a vital role in the clean energy transition by utilizing its vast thorium reserves.⁶ A variety of design concepts are proposed using the molten salt mixture as the fuel for a reactor in the form of metal fluorides or chlorides.^{1–6} The spent fuel hosts multiple elements in various oxidation states with different levels of radioactivity. In the closed fuel cycle, the reprocessing of spent fuel based on the MSR would generate nuclear wastes containing fluorides. The rare earths and zirconium are the principal fission products removed from earlier MSR reprocessing plants.^{7,8} Around the globe, borosilicate glasses are the most preferred choice for the immobilization of high-level waste (HLW).⁹ The ability to accommodate various metal ions of different oxidation states along with high loading capacity in chemically durable form makes glasses a unanimous choice for interim storage of HLW.¹⁰ Despite these beneficial properties, some key issues such as volatilization of Tc and Cs fission products and the negative effect of high temperature on leaching under

geological conditions still remain to be addressed.¹¹ Fluorides containing wastes are volatilized as SiF_4 during borosilicate glass fabrications.⁸ Moreover, the accommodation of trivalent and tetravalent actinides, generated in the reactor, also has limited solubility in glasses which leads to the separation of crystalline phases at higher loading.¹² The long-term durability issues are also rarely addressed or known for actinides-containing glasses that are thermodynamically metastable.¹² Interestingly, ceramics have emerged as thermodynamically stable HLW waste forms and have superior properties over glasses such as higher long-term durability, better-leaching resistance as well as radiation resistance.¹² As compared to glass, the only limitation of ceramic waste forms is to incorporate various metal ions in a predefined stoichiometric composition of ceramic structure in a single phase.¹² To circumvent the issue of accommodating various metal ions in

Received: May 22, 2024
Revised: July 18, 2024
Accepted: July 23, 2024
Published: August 10, 2024



different phases, a multiphase assemblage of various phases like Synroc, has been proposed and demonstrated for HLW immobilization.⁹ The choice of a suitable phase is dependent upon the solubility of metal ions in a particular phase without disrupting the original crystal structure.⁹ Even, single-phase waste forms such as monazite and zircon are proposed for the immobilization of actinides and lanthanides.⁹ Several ceramics waste forms such as pyrochlores, phosphates, silicates, and perovskites have improved thermodynamic stability, and radiation resistance nature as compared to borosilicate glasses.^{8,9} Ceramics, as mentioned above, usually show superior thermodynamic stability than glass matrices due to their crystallographic stability.^{13–17} McCarthy pointed out a higher leaching rate at repository conditions in glasses.^{15,16,18} They have proposed that radioactive waste can be incorporated into ceramic materials composed of crystalline phases.¹⁸ Moreover, glasses are metastable in nature due to high-temperature ordering.^{18–20} To have the best of both materials, researchers even suggested the use of glass-bonded ceramics to incorporate useful properties of both glass and ceramics for better safeguarding.²¹ Irrespective of the type of waste forms, structural stability against temperature, pressure, and radiation are the most important aspects to be investigated thoroughly for better assessment of the waste matrix under a geological repository. The temperature of the geological repository may increase due to sudden external geothermal effects. Hence, temporal profiling of waste forms should be examined exhaustively for any proposed matrix. Apart from temperature, the effect of pressure on the structure and physical properties of waste forms is required to validate their possible use in nuclear waste repositories. In particular, high-pressure studies are also highly relevant for assessing the mechanical stability of nuclear waste forms in relation to processing techniques like Hot Isostatic Pressing (HIP). Recent research on high-pressure studies clearly demonstrates the importance of pressure-induced changes on ceramic materials.^{22,23} Pressure can induce structural phase transitions and disorders, which can provide insight into altered atomic arrangements. Radiation-induced damages like metamictization are also important to investigate due to the loss of long-range structural order in ceramic waste forms, which in turn affects the properties.

For halide-based wastes, ceramic waste forms are more promising than glasses due to the higher loading of fluorides, nonvolatilization as well as chemical and thermodynamic superiority.⁸ For halides, the most prominent ceramic waste forms are sodalite; $A_8(\text{AlSiO}_4)_6\text{X}_2$ where A is a monovalent metal ion and X is a halide and haloapatites; $B_{10}(\text{PO}_4)_3\text{X}_2$ where B is a divalent metal ion.⁸ Out of these two promising waste forms, apatites have more flexibility to incorporate various metal ions with different oxidation states with charge-coupled substitution.^{24,25} Moreover, fluoride incorporation in sodalite is difficult and has rarely been reported. The most studied fluorapatites (FAPs) for immobilization of radioactive wastes are $\text{Ca}_{10}(\text{PO}_4)_6\text{F}_2$ (CaFAP) and $\text{Sr}_{10}(\text{PO}_4)_6\text{F}_2$ (SrFAP). Recently, our group has shown that CaFAP is more resistant to β^- radiation as compared to SrFAP.²⁴ The charge-coupled substitution of the type $2\text{Ca}^{2+} \rightarrow \text{A}^+ + \text{Ln}^{3+}$ (where A is a monovalent ion and Ln is a lanthanide ion) in CaFAP has been shown to be a successful strategy to incorporate monovalent and trivalent ions in the FAP matrix along with fluorides.²⁵ Calcium ion in FAP structure has a very flexible coordination polyhedron.²⁴ CaFAP crystallizes in a hexagonal lattice with space group $P6_3/m$. There are two sites of calcium in the

CaFAP lattice, one is nine-coordinated (Ca1) and the other is seven-coordinated (Ca2), having fluorine at one of the apexes of the Ca2 site.^{24,25} The occupancy of calcium at two sites, Ca1 and Ca2 are 0.4 and 0.6, respectively.^{24–26} The substituted ions for Ca^{2+} , based on their charge and size, can be distributed between these two sites and, hence, may change the thermodynamic stability of the FAP matrix.^{24–26} It is imperative to study the thermophysical properties as well as the thermodynamic behavior of Ln^{3+} -substituted CaFAP. The previous structural studies on the lanthanide-substituted CaFAP matrix have confirmed that Ln^{3+} ions preferentially occupy the Ca2 site while monovalent ions like Na^+ exclusively occupy the nine coordinated Ca1 site.^{24–26} Charge-coupled Ln^{3+} substituted CaFAP are not only applied in view of HLW waste forms but also reported to have interesting properties such as photoluminescence, magnetism, etc.^{26–30} Although Ln^{3+} substitution overall does not change the space group of CaFAP, the occupation of Ln^{3+} between two sites is a function of the concentration of lanthanide, as shown in our recent work, where the occupancy of Eu^{3+} between two sites, namely, Ca1 and Ca2, depends upon the concentration of Eu^{3+} in CaFAP.¹⁴ Most of the Ln^{3+} -substituted fluorapatite are reported with a very low concentration (1–5%) range where occupancies between these sites were not refined or not necessary for the applications studied.^{27–30} To delineate the effect of different Ln^{3+} ions on the structural and thermophysical properties of substituted fluorapatites, we have synthesized a range of Ln^{3+} charge-coupled substituted CaFAP (where $\text{Ln}^{3+} = \text{La}^{3+}$ to Lu^{3+} except Pm^{3+}) in the present work. Moreover, as a waste form, the matrix must be capable of substituting multiple ions in a single phase.³¹ To prove this feasibility, we also synthesized multilanthanide-doped CaFAP in a single phase, and its structural and thermodynamic properties were correlated with single lanthanide-substituted CaFAP analogs.

EXPERIMENTAL SECTION

Synthesis of $\text{NaLnCa}_8(\text{PO}_4)_6\text{F}_2$ ($\text{Ln} = \text{La}$ to Lu Except Pm) Solid Solutions. Calcium carbonate (CaCO_3), lanthanum oxides (general formula Ln_2O_3), sodium nitrate (NaNO_3), ammonium dihydrogen phosphate ($\text{NH}_4\text{H}_2\text{PO}_4$), and ammonium bifluoride (NH_4HF_2) were purchased from Alfa Aesar and have been used for the compound preparation. Stoichiometric ratios of CaCO_3 , Ln_2O_3 (except Pr and Tb), NaNO_3 , $\text{NH}_4\text{H}_2\text{PO}_4$, and a slight excess of NH_4HF_2 (1.2 mol % in order to avoid fluorine losses) were mixed thoroughly in agate mortar with few drops of ethanol for proper homogenization. In the case of praseodymium and terbium, Pr_6O_{11} and Tb_4O_7 are taken instead of Ln_2O_3 as starting precursors, respectively. The mixtures were heated initially at 473 K for 3 h and then at 773 K for 12 h, 973 K for 24 h, and 1223 K for 48 h. The final products were again ground and stored in desiccators for further characterization. In the case of multilanthanide doping, all the lanthanide oxides were taken in an equal stoichiometric ratio such that the total Ln content is 10 atom % in the synthesized compound.

INSTRUMENTATION AND MEASUREMENTS

X-ray Diffraction (XRD). The synthesized compounds were characterized by XRD analysis in a Rigaku Smartlab diffractometer using $\text{Cu } K_\alpha$ radiation ($\lambda = 1.5406 \text{ \AA}$) in the 2θ range of $10\text{--}100^\circ$ with a step size of 0.02° (2θ) and a counting

time of 5 s per step. The phase purity of the desired compounds was analyzed by comparing the obtained XRD patterns with the reported data of CaFap hexagonal phase.^{13,14} For the structural elucidation, the obtained XRD patterns of the compounds were refined by the Rietveld refinement method using the Fullprof suite computer program.^{32,33} For the structural analysis, we used the background with a Chebyshev polynomial function. To model the shape of the peaks, we employed a pseudo-Voigt function along with Cagliotti coefficients. The refinement of atomic occupation was carried out by considering the initial stoichiometry and crystal sites. Isotropic refinement was performed to refine the thermal parameters. High-temperature XRD measurements of the samples were carried out by Rigaku HT 1500 attachment in the range of 298–1073 K in the same instrument.

Microhomogeneity Analysis of NaSmCa₈(PO₄)₆F₂ and NaLnCa₈(PO₄)₆F₂ Solid Solutions. The micro homogeneity of synthesized fluorapatite solid solutions for NaLnCa₈(PO₄)₆F₂ and NaSmCa₈(PO₄)₆F₂ was confirmed through SEM-EDS studies. Both samples were examined for surface morphology using a tungsten filament-based scanning electron microscope (SEM Model: AIS 2100, M/s. Seron Inc., Korea) with an acceleration voltage of 20 kV.³⁴ Furthermore, elemental analysis was conducted using an energy dispersive spectrometer (EDS) (Model: INCA E350, M/s. Oxford Instruments, UK), which was calibrated using high-purity electro-polished cobalt.³⁴ Lighter element contents were not quantified from these results since the EDS detector demonstrated poor sensitivity toward lighter elements with atomic numbers below 11.

Infrared and Raman Spectroscopic Study. Platinum ATR (by Bruker alpha, single reflection Diamond crystal, all reflective, gold-coated optics, no fragile composite material construction) within the spectral range 5000–500 cm⁻¹ was used to study the vibrational characteristics of functional groups present in the compounds.^{24,25} The resolution of the IR instrument is 4 cm⁻¹.

Raman spectra of all the samples were recorded on a micro-Raman LabRAMHR-800 evolution instrument by using 633/532 nm LASER of power 10 mW. A 50X objective lens (Olympus) was used to focus the light onto the samples.^{24,25} The same objective lens was used to collect the scattered light. Since the spectra recorded with 532 nm contained fluorescence peaks, we have reported the Raman spectra in the manuscript only by 633 nm. The backscattered lights were resolved using 600 lines/mm grating which gives spectral coverage of 1.2 cm⁻¹ per pixel.

Heat Capacity. Isobaric molar heat capacities of the solid solutions NaLnCa₈(PO₄)₆F₂ (Ln = Pr to Ho except Pm) were measured experimentally by heat flux type differential scanning calorimetry using model number DSC 1/700 of M/s. Mettler Toledo GmbH, Switzerland.^{24,25} These experiments were carried out in the temperature range of 300–865 K under a constant flow of high-purity (99.999%) argon as a carrier gas. The oxygen impurity below 10 ppm in the carrier gas was maintained by passing it through various oxygen and moisture traps, and its purity was further confirmed by solid-state oxygen sensors attached to the mass control box. A classical three-step method with a continuous heating mode was used for the measurement of heat capacities. A thin disc of α -Al₂O₃ (SRM 720)^{24,25} was used as the reference material. Heat flow was recorded as a function of temperature at a constant heating rate of 5 K/min, while the flow rate of the carrier gas was

maintained at 20 mL/min. To minimize the random errors, five cycles were run for each compound, and averages of the heat flow signals obtained in the cycles were taken for heat capacity measurements.

Enthalpy Increments and Enthalpy of Dissolution. A high-temperature Calvet type calorimeter (AlexSYS 1000, M/s. SETARAM, France) was used for measuring the enthalpy increments ($\Delta H_{298,m}^T$) and enthalpies of dissolution. The measurements were done in the temperature range 690–1115 K under a high purity (99.999%) argon atmosphere. The detailed instrumental description and the measurement setup are reported elsewhere.²⁴ Calibration of the heat signals was carried out at each experimental temperature by dropping NBS standard, α -Al₂O₃ (SRM 720). Typically about 10–20 mg weight of sample pieces and 20–30 mg of sapphire pieces were taken for the measurements. To ensure the reproducibility of the data, three pieces of the reference material as well as the sample were dropped at each temperature. Following eq 1 has been used for the calculation of enthalpy increments:

$$\Delta_{298.15}^T H_m^0(S) = \Delta_{298.15}^T H_m^0(R) \times \frac{\int_0^t (\phi_S - \phi_B) d\tau}{\int_0^t (\phi_R - \phi_B) d\tau} \times \frac{M_S}{m_S} \times \frac{m_R}{M_R} \quad (1)$$

where $\Delta H_{298,m}^T(S)$ and $\Delta H_{298,m}^T(R)$ are the molar enthalpy increments of the sample and the reference material (α -Al₂O₃ in this case) respectively. ϕ_B is the equilibrium state heat flux i.e., baseline while ϕ_S and ϕ_R are the heat flux after the addition of the sample and the reference materials, respectively. The integrals $\int_0^t (\phi_S - \phi_B) d\tau$ and $\int_0^t (\phi_R - \phi_B) d\tau$ are the peak areas corresponding to the enthalpy increments of the sample and the reference materials, respectively. m_S and m_R are the weights of the sample and the reference materials, respectively, whereas M_S and M_R are their molar masses.

To measure the enthalpy of dissolution, 2PbO:B₂O₃ was used as the solvent medium. However, Westrich and Navrotsky have shown that the solubility of these fluorides is very limited in (2PbO: B₂O₃) solvents. Therefore, AlF₃ was added as an additive in samples in a 1:2 molar ratio since the faster dissolution of AlF₃ enhanced the dissolution of the samples.³⁵

Radiation Stability Study by Electron Beam. The irradiation experiments were carried out with 10 MeV electron beams in pulsed mode at the indigenously developed Linear Accelerator (LINAC) housed at the Electron Beam Centre, BARC. A detailed description of the system developed is provided in earlier work.³⁶ The beam pulses exited through a 1 m long titanium exit window and scanned over the fluorapatite samples kept at room temperature under normal light conditions and an ambient atmosphere. The powder specimens were wrapped in Al foil of thickness ~75 μ m to avoid any spillage. The range of 10 MeV electrons in Al is 1.92 cm, and hence, they can easily pass through the Al foil with negligible absorption. The calibrated dose per pulse was calculated as 1 MGy/h at 20 cm from the source window before irradiation with a 2.4 kW beam source. Cumulative doses of 1 MGy and 20 MGy were used to irradiate all the samples.

X-ray Absorption Spectroscopy Studies. An X-ray absorption spectroscopy (XAS) measurement, which comprises both X-ray near edge structure (XANES) and extended X-ray absorption fine structure (EXAFS) techniques, has been carried out on unirradiated and electron beam irradiated NaLnCa₈(PO₄)₆F₂ samples (1 and 20 MGy) (Ln = Pr–Ho) at

Ln L_3 -edges to study local structural distortion induced by electron radiations. The XAS measurements in transmission mode have been carried out at the energy-scanning EXAFS beamline (BL-9) at the Indus-2 Synchrotron Source (2.5 GeV, 100 mA) at Raja Ramanna Centre for Advanced Technology (RRCAT), Indore, India.^{37,38}

RESULTS AND DISCUSSION

Structural and X-ray Diffraction Studies. Charge-coupled substitution in CaFAP ($\text{NaLnCa}_8(\text{PO}_4)_6\text{F}_2$) was carried out as per the following equation:



The compounds were synthesized by conventional solid-state reactions with 10 at. % Ln^{3+} and Na^+ ions in a CaFAP matrix. Powder XRD patterns were recorded and are shown in Figure 1. All Ln-substituted CaFAP with Ln = Pr to Ho

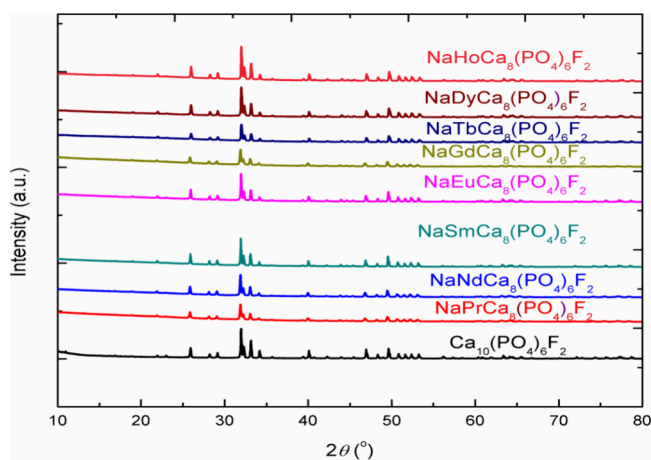


Figure 1. Powder XRD patterns of the $\text{NaLnCa}_8(\text{PO}_4)_6\text{F}_2$ solid solutions.

crystallize in the hexagonal apatite phase. The absence of additional XRD peaks except for the desired fluorapatite phase (where Ln = Pr–Ho except Pm) in the XRD patterns shows that no alteration in the crystal lattice of the hexagonal phase, as well as no separate phase, was formed after Na^+ and Ln^{3+} ion substitution in CaFAP. On the contrary, compositions containing La^{3+} , Ce^{3+} , and Er^{3+} – Lu^{3+} were not phase-pure under the synthetic conditions used in the present study (Figure S1). Similar findings were reported by Mayer et al.³⁹ where pure phase was not reported for Er–Lu-containing fluorapatites due to size limitation in the substitution of Ln^{3+} at the Ca site. Kreidler and Hummel et al.⁴⁰ also predicted the crystal stability based on the size of the ions to be substituted. According to their calculations, the ionic radii for the ions (Re) substituting Ca in fluorapatites were found to be $0.95 \text{ \AA} < \text{Re} < 1.35 \text{ \AA}$.^{39–41} The Er^{3+} ionic radius in seven coordination (0.945 \AA) is lesser than 0.95 \AA and hence the fluorapatite phase after substituting late lanthanides (Er–Lu) (i.e., Tm–Lu) at seven coordinated Ca site is not stable.^{39–41} These ionic radii limits set the lower and upper bounds of lanthanide elements which can be incorporated in the CaFAP matrix in a charge couple fashion with Na^+ to give phase pure compounds. Interestingly, the impurity phases observed in the XRD patterns were different for early (La^{3+} and Ce^{3+}) and late lanthanides (Er^{3+} – Lu^{3+}). In the case of La^{3+} and Ce^{3+} substitution, the monazite phase of LnPO_4 (space group, P

$2_1/n$) was observed along with the fluorapatite phase while major impurity phases, observed for late lanthanides (Tm, Yb, and Lu) substitution were $\text{Ca}_3(\text{PO}_4)_2$ (space group $R\bar{3}m$) and xenotime LnPO_4 (space group $I4_1/amd$) except for Er, where we got Er_2O_3 also as a minor phase. The peaks in XRD patterns of pure phases (Pr–Ho) show a continuous shift toward higher angles (Figure 2) due to a reduction in the ionic

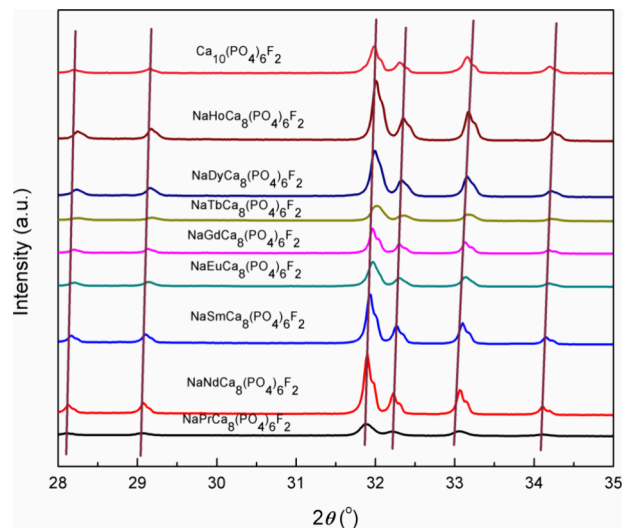


Figure 2. Enlarged XRD patterns of $\text{NaLnCa}_8(\text{PO}_4)_6\text{F}_2$ solid solutions.

radius of Ln^{3+} ions from Pr to Ho. This resulted in the lattice contraction from Pr to Ho as evidenced by the lattice parameter values obtained from Rietveld refinement (vide infra).

As stated earlier, in the CaFAP lattice, there are two cationic sites, namely, Ca1 and Ca2 (Structure of CaFAP). The Ca1 site is nine coordinated forming a CaO_9 polyhedron with nine oxygen atoms from the phosphate groups while the Ca2 site is seven coordinated with one fluorine atom and six oxygen atoms forming a CaO_6F polyhedron. The occupancies of cations at these two sites are 0.4 and 0.6 for Ca1 and Ca2 sites, respectively. Recently, our group reported structural and thermophysical properties of Eu^{3+} and Na^+ charge-coupled substituted CaFAP fluorapatites in which Eu^{3+} mostly remained at the Ca2 site (80%) while Na^+ was substituted at Ca1 sites.²⁵ To study the effect of different lanthanide substitutions on the structure of CaFAP, Rietveld refinement of all the phase pure compounds was carried out in a similar manner. For refinement, CaFAP ($\text{Ca}_{10}(\text{PO}_4)_6\text{F}_2$) was taken as an initial model compound with the $P6_3/m$ space group. It is well reported that monovalent ions like Na^+ are exclusively substituted at the Ca1 site in substituted CaFAP (CaFAP structure).^{24–26,42,43} Hence, during refinement of occupancies, the Na^+ ion was retained at the Ca1 site. Occupancies of substituted Ln^{3+} ions were refined between two sites, namely, Ca1 and Ca2, by the trial and error method to minimize the χ^2 values. While refining the occupancy values, all other parameters were kept fixed. Moreover, the total amount of Ca^{2+} , Na^+ , and Ln^{3+} was kept constant according to the formula unit of these solid solutions as well as total metal ion occupancies at Ca1 and Ca2 sites were also fixed at 0.4 and 0.6, respectively, according to the initial model of $\text{Ca}_{10}(\text{PO}_4)_6\text{F}_2$. The χ^2 values with occupancies are given in Table S1. The χ^2

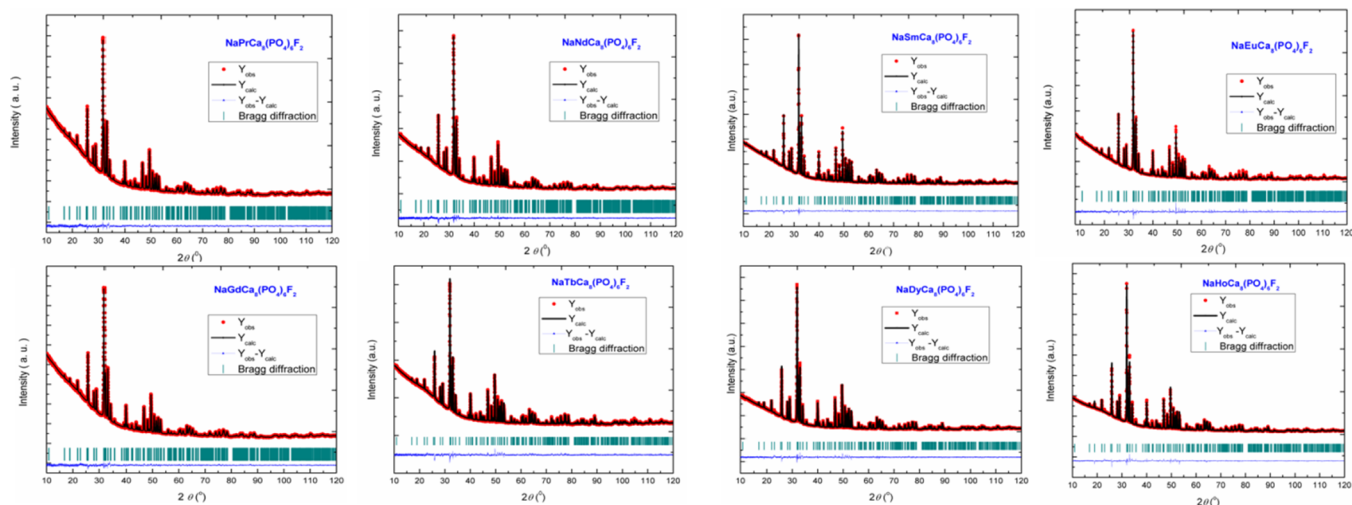


Figure 3. Rietveld refinement patterns of $\text{NaLnCa}_8(\text{PO}_4)_6\text{F}_2$ solid solutions (Pr–Ho except for Pm).

Table 1. Fitting Parameters of the Synthesized Solid Solutions after Rietveld Refinement

parameters	Pr	Nd	Sm	Eu	Gd	Tb	Dy	Ho
$\text{NaLnCa}_8(\text{PO}_4)_6\text{F}_2$								
$a = b$ (Å)	9.3972(1)	9.3909(1)	9.3857(1)	9.3796(1)	9.3744(1)	9.3728(1)	9.3716(1)	9.3629(1)
c (Å)	6.9031(1)	6.8986(1)	6.8917(1)	6.8878(1)	6.8827(1)	6.8796(1)	6.8792(1)	6.8703(1)
volume (Å ³)	527.92(1)	526.88(1)	525.76(1)	524.78(1)	523.81(1)	523.40(1)	523.23(1)	521.59(1)
2θ -range (°)	10–120°	10–120°	10–120°	10–120°	10–120°	10–120°	10–120°	10–120°
R_{wp} (%)	2.35	3.29	2.60	2.39	2.47	3.40	2.16	2.32
R_{exp} (%)	2.20	1.51	1.40	1.82	1.75	2.57	1.24	1.30
χ^2 (%)	1.13	4.75	3.47	1.73	2.00	1.75	3.02	3.16

values with occupancies are given in Table S1. Figure 3 shows the final fit of Rietveld refinement for all of the Ln^{3+} substituted compositions. The lattice parameters as well as fitting parameters are shown in Table 1. The lattice parameter of the synthesized solid solutions was plotted with the Ln^{3+} ionic radius and has been shown in Figure 4, following a decreasing trend from Pr–Ho. The occupancy values in Figure 4 show that Ln^{3+} ions are preferentially substituted at the Ca2 site as compared to the Ca1 site. The preference of Ln^{3+} for the Ca2 site is due to lower ionic radii of Ln^{3+} as compared to the Ca^{2+} as well as stronger bonding with F^- ion as compared

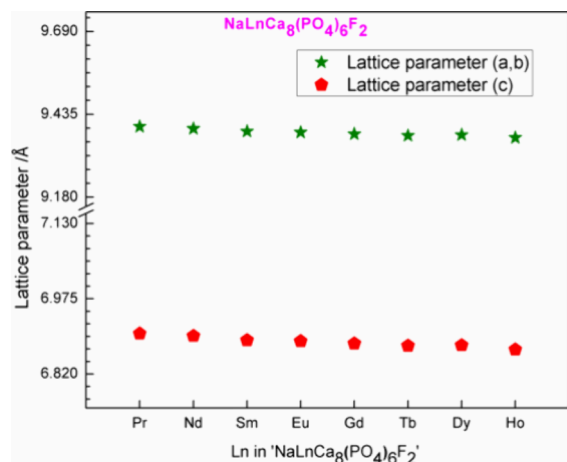


Figure 4. Variation of lattice parameter with different lanthanides in $\text{NaLnCa}_8(\text{PO}_4)_6\text{F}_2$ solid solutions.

to oxide ions. It is evident from Figure 5 and Table S1 that the occupation of lanthanides at two sites does not follow the

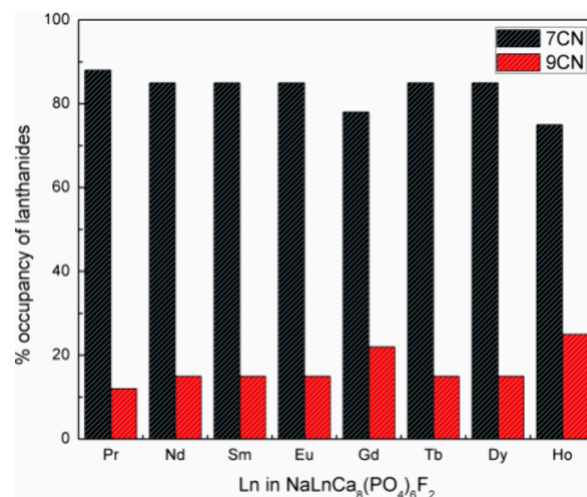


Figure 5. Occupancy of Ln^{3+} ions on the Ca1 site (9 coordination numbers-9CN) and Ca2 site (7 coordination numbers-7CN).

trend of ionic radii of lanthanide ions. In early lanthanides (up to Eu^{3+}), the occupation value at the Ca2 site is almost 85% while at Gd^{3+} this value comes down to 78%. Further in Ho^{3+} also, this value is 75%. This suggests that among the lanthanides, early lanthanides (Pr³⁺–Eu³⁺) slightly favor the Ca2 site as compared to the Ca1 site. Fluorapatite structures after cation substitution can transform to lower symmetries, as indicated by White et al.⁴⁴ They have proposed that a

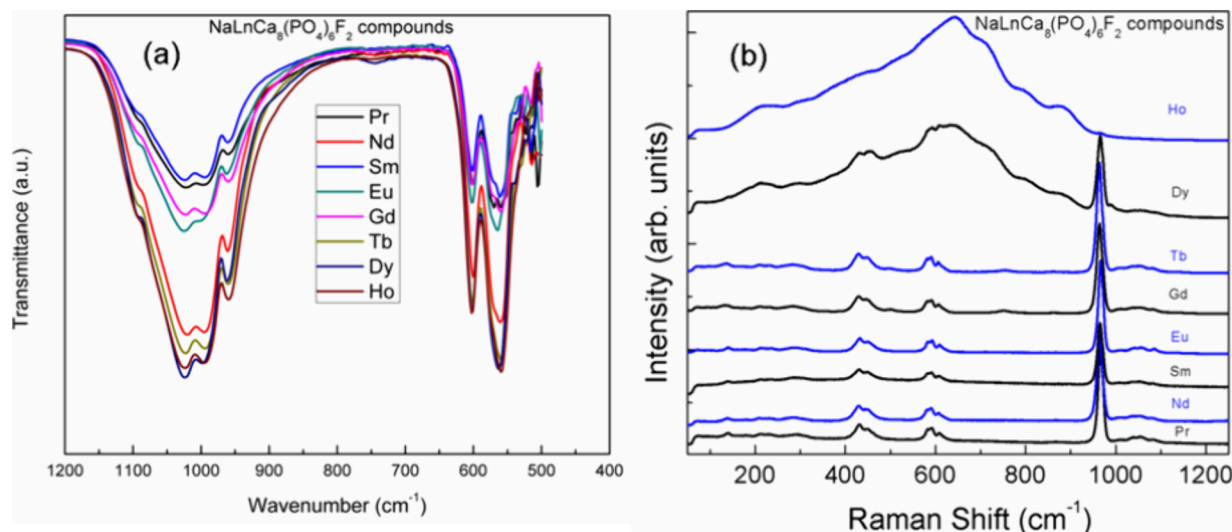


Figure 6. (a) IR and (b) Raman spectra of $\text{NaLnCa}_8(\text{PO}_4)_6\text{F}_2$ solid solutions (Pr–Ho except Pm).

fluorapatite structure can be visualized as a $\text{Ca}(1)\text{O}_6$ metaprism framework with corner-shared PO_4 units, and in the channel, there is embedded $\text{Ca}(\text{II})_6\text{F}_2$. In these structures, the metaprism twist angle ϕ shown in Figure S2 gives a qualitative idea for crystallization in the $\text{P6}_3/\text{m}$ space group for fluorapatite.^{44,45} The ϕ values should be between 5° and 25° for a composition to remain in an apatite structure ($\text{P6}_3/\text{m}$) with distortion. This distortion may be due to substitution at cationic or anionic sites in the fluorapatite structure. The ϕ values for our compounds were calculated and are plotted in Figure S3. All the values lie between 23° and 25° . This also confirms that all the charge-coupled substituted CaFAP synthesized in this work crystallizes in the $\text{P6}_3/\text{m}$ space group without any long-range structural change. The important bond lengths for all the compositions are tabulated in Table S2.

Microhomogeneity Analysis of $\text{NaSmCa}_8(\text{PO}_4)_6\text{F}_2$ Solid Solutions. SEM–EDS analysis was conducted on mono lanthanide substituted sample $\text{NaSmCa}_8(\text{PO}_4)_6\text{F}_2$. SEM images at different resolutions are shown in Figures S3 and S4. In order to perform EDS elemental analysis, three distinct zones were chosen for the sample. For all three zones, ratios of Ca to Sm were calculated and shown in Figure S5 along with SEM images and EDS spectra. It can be easily observed from the EDS study that the sodium peaks are also observed on the elevated background of the Bremsstrahlung radiation in the region. Hence, we calculated only the Ca to Sm ratio at different zones. The obtained ratio of Ca to Sm from EDS elemental analysis corroborated well with the reported bulk stoichiometry. The authors have previously conducted experimental measurements to determine the total content of F, Na, and P in Eu-doped fluorapatite samples.⁴⁶ These studies show that the sample is homogeneous in nature.

Infrared and Raman Studies. According to group theory analysis, isolated phosphate PO_4^{3-} with T_d symmetry consists of the following mode of vibrations expressed by eq 3:

$$A_1(\text{R}) + E(\text{R}) + 2E_2(\text{I.R., R}) \quad (\text{where R} = \text{Raman and I.R.} = \text{infrared}) \quad (3)$$

The fundamental tetrahedral symmetry of the free phosphate group (T_d) further becomes nondegenerate due to the existence of surrounding atoms in the case of the apatite

structure. Hence IR and Raman spectra of apatite are different as expected from group theory calculation of free phosphate groups. The factor group analysis of fluorapatite with the $\text{P6}_3/\text{m}$ space group⁴⁷ shows that the total internal mode of vibration can be represented by eq 4

$$\Gamma = 6A_g + 6E_{2g} + 6B_u + 6E_{1u} + 3B_g + 3E_{1g} + 3A_u + 3E_{2u} \quad (4)$$

where E is doubly degenerate.

Out of these internal vibrations, the Raman active vibrations and IR active vibrations for PO_4^{3-} groups are

$$\Gamma_{\text{Raman}} = 6A_g + 6E_{2g} + 3E_{1g} \quad (5)$$

$$\Gamma_{\text{IR}} = 3A_u + 6E_{1u} \quad (6)$$

Therefore, a total of 15 Raman vibration peaks and 9 IR vibration peaks could be assigned to internal modes of vibrations.

In the free PO_4^{3-} group, two triply degenerate infrared modes are located at $1000\text{--}1100\text{ cm}^{-1}$ (the P–O asymmetric stretching: ν_3 (f_2)) and $500\text{--}570\text{ cm}^{-1}$ (the P–O bending: ν_4 (f_2)). Raman active bands located at $\sim 940\text{ cm}^{-1}$ (singlet symmetric P–O stretching mode: ν_1 (a_1)) and at $420\text{--}350\text{ cm}^{-1}$ doubly degenerate O–P–O deformation: (ν_2 (e)) completes the vibrational spectra.^{24,25,48} In the fluorapatite structure, the PO_4^{3-} group is situated at the C_s site and factor group analysis by Baddiel et al. shows that a total of 9 active fundamental modes of vibration become IR active.⁴⁸ Both the two triply degenerate modes (ν_3 and ν_4) become non-degenerate whereas ν_1 and ν_2 modes also become I.R. active under the factor group. FTIR spectra of all of the synthesized compounds (Pr–Ho) are shown in Figure 6a. The obtained peaks are given in Table S3. In the FTIR spectra, ν_1 , ν_3 , and ν_4 models are visible while ν_2 is not seen as the frequency is outside the operating window of the FTIR instrument used in this study ($500\text{--}4000\text{ cm}^{-1}$). The ν_3 bands, asymmetric stretching vibrations of the PO_4^{3-} group in fluorapatite, are observed at $1092\text{--}1097\text{ cm}^{-1}$ (weak shoulder), $1027\text{--}1021\text{ cm}^{-1}$ (strong peak), and $992\text{--}999\text{ cm}^{-1}$ (strong peak). In calcium fluorapatite, CaFAP, the two peaks (~ 1025 and $\sim 992\text{ cm}^{-1}$) are not well resolved and observed as a single broad peak.²⁵ The observance of two distinct peaks in sodium and

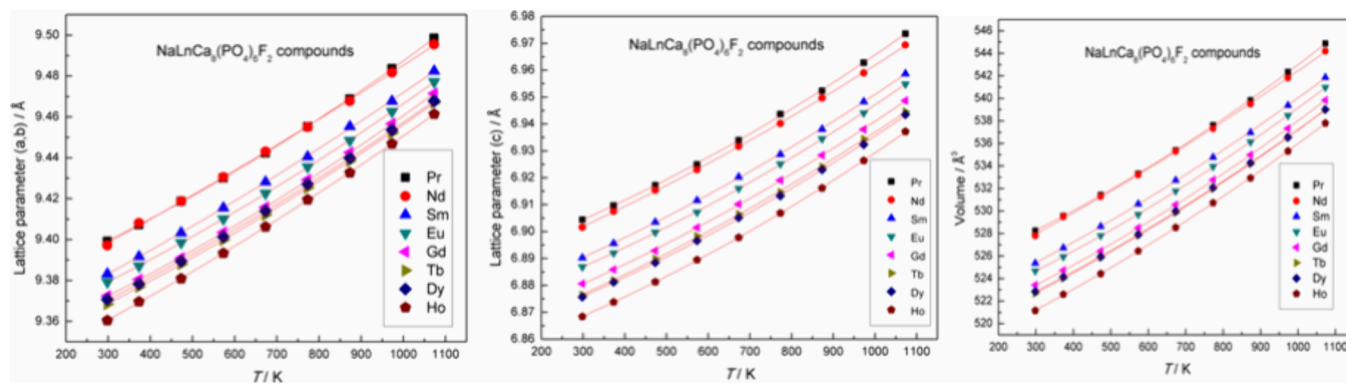


Figure 7. Variation of lattice parameters of $\text{NaLnCa}_8(\text{PO}_4)_6\text{F}_2$ solid solutions as a function of temperature.

lanthanide cosubstituted CaFAp might be due to the different connectivity of phosphate to lanthanide ion, calcium ion, and sodium ion. The symmetric stretch ν_1 is observed at 959 cm^{-1} which was IR-forbidden in isolated tetrahedral PO_4^{3-} . The ν_4 bands are observed at $600\text{--}602\text{ cm}^{-1}$ (strong peak), $569\text{--}573\text{ cm}^{-1}$ (weak shoulder), and $558\text{--}567\text{ cm}^{-1}$ (strong peak) which is a nondegenerate triplet in CaFAp (P_{63}/m) similar to the ν_3 band. This weak shoulder of $\sim 573\text{ cm}^{-1}$ was also not observed in CaFAp. This FTIR study suggests that lanthanide and sodium charge-coupled substitution in CaFAp gives rise to more distortion in the coordinating PO_4^{3-} group in terms of different connecting metal ions (Ln^{3+} , Ca^{2+} , and Na^+) to oxygen atoms of the PO_4^{3-} group.

Raman spectra of the solid solutions are also shown in Figure 6b along with the IR spectra. As discussed above, the ν_1 mode is observed as a single peak in the range of $963\text{--}966\text{ cm}^{-1}$ for the Ln-substituted fluorapatite. The ν_3 mode which is Raman inactive in isolated tetrahedral PO_4^{3-} is observed as a weak broad band in these fluorapatites due to the C_s site in the range of $1050\text{--}1087\text{ cm}^{-1}$. The ν_2 Raman active mode is split into doublet and is observed in the range of $448\text{--}455\text{ cm}^{-1}$ and $428\text{--}431\text{ cm}^{-1}$. Similarly, the ν_4 band is observed as broad triplets in the range of $602\text{--}570\text{ cm}^{-1}$. These Raman and FTIR observations show that after lanthanide substitution there is no major difference in the local structure of the phosphate group which in turn corroborates the results of XRD studies that there is no significant departure from the structure of CaFAp upon lanthanide substitution.

High-Temperature X-ray Diffraction. Thermal expansion is the most important property that directly correlates to the storage of radioactive waste from under the geological repository, having a temperature rise due to decay heat.^{24,25} Moreover, thermal stability is also related to the leaching resistance of the waste form under geological burial of waste forms.^{24,25} To understand the thermal behavior of lanthanide-substituted CaFAp, high-temperature XRD was used to determine the associated changes in the crystal structure. Figure S6 shows the powder XRD patterns of Ln-substituted CaFAp within the temperature range $298\text{--}1073\text{ K}$. It is obvious that these Ln-substituted CaFAp are stable in the temperature range studied as no additional peaks appeared in XRD patterns at elevated temperatures. To get an insight into the structural changes with temperature, Rietveld refinement of XRD patterns with temperature was carried out. Figure S7 shows the Rietveld refinement fit of HT-XRD patterns of $\text{NaLnCa}_8(\text{PO}_4)_6\text{F}_2$ compounds at 1073 K . Lattice parameters and volume of unit cells thus obtained were plotted with

respect to temperature in Figure 7. The lattice parameters and volumes were fitted with the polynomial of the type of eq 7

$$\text{L.P. or } V = A + BT + CT^2 \quad (7)$$

where L.P. are lattice parameters; V is the volume; A , B , and C are the coefficients; and T is the temperature. The values of $A\text{--}C$ are given in Table S4. It can be seen from Figure 7 that all the compounds show positive thermal expansion upon heating. The c/a ratio was also plotted and is shown in Figure S8. From Figure S8, it is clear that there exists an inverse relationship between the c/a ratio and temperature. A similar observation was also observed in the case of CaFAp and SrFAp.²⁴ This is due to the more closely packed structure along the c -axis as compared to the a - or b -axis in the fluorapatite structure.⁴⁹

From the definition of thermal expansivity, $\alpha_V = 1/V(dV/dT)_P$, volume at T can be derived as $V_T = V_{298} \exp(\int_{298}^T \alpha_V dT)$, where V_{298} is the volume at 298 K . If α_V is considered as a linear function of T , $\alpha_V = A + BT$, then V_T can be represented as $V_T/V_{298} = \exp[A(T - 298) + B(T^2 - 298^2)/2]$. We have plotted V_T/V_{298} as a function of T and fitted by the least-square method. Similar to the volume thermal expansivity, the lattice thermal expansivities (α_a and α_c) were also calculated. The fitted values of A and B are given in Table S5. The volume thermal expansivity against temperature is plotted in Figure 8. It is obvious from the figure that as the temperature increases, there is no monotonic trend in volume thermal expansivity as we go from Pr to Ho. After a particular temperature, the expansivity plots cross each other. The general trend in these

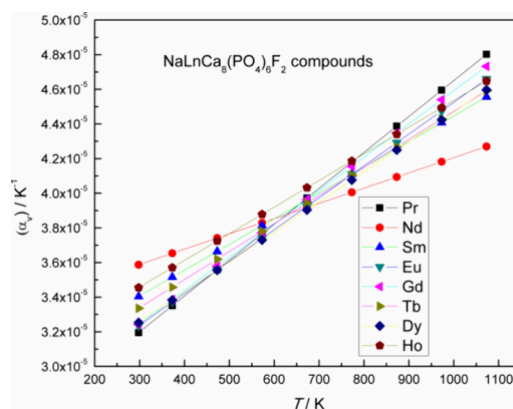


Figure 8. Volume thermal expansivity vs temperature of $\text{NaLnCa}_8(\text{PO}_4)_6\text{F}_2$ solid solutions.

plots signifies that although the thermal expansivity increases with temperature for all compositions, the compositions which are having smaller values of expansivity at lower temperatures have larger values at higher temperatures. This observation clearly confirms the different anharmonicity strengths of Ln-O bonds in different lanthanide-doped CaFap. To probe the anisotropy in expansivity, the ratio of lattice thermal expansivities along different axes (α_a/α_c) were plotted with respect to temperature in Figure 9. The ratio of expansivities

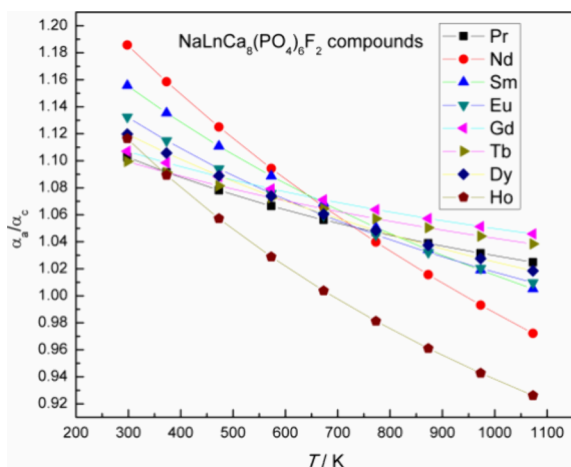


Figure 9. Anisotropy in lattice thermal expansivity vs temperature of $\text{NaLnCa}_8(\text{PO}_4)_6\text{F}_2$ solid solutions.

shows that as the temperature increases, the anisotropy in expansivities decreases and approaches near to one in all compounds except those of Pr and Ho. In Pr and Ho, first anisotropy in expansivities decreases and then increases in reverse order at higher temperatures. A similar anisotropy behavior was observed in lanthanide-doped oxyapatite³¹ and correlated this observation with the migration of lanthanide ions between the Ca1 site and the Ca2 site at higher temperatures. Moreover, the room temperature instantaneous volume thermal expansivity values of these compounds vary from 3.1×10^{-5} to $3.6 \times 10^{-5} \text{ K}^{-1}$ which is close to the value for CaFap ($3.1 \times 10^{-5} \text{ K}^{-1}$). Moreover, these values of instantaneous volume thermal expansivity are similar to the other reported oxyapatite waste forms.³¹

Thermodynamic Studies. Heat capacity is an important thermodynamic property that correlates to the different thermodynamic functions like enthalpy and entropy. To predict a thermodynamic stability criteria, one needs to have these parameters. In view of this, heat capacities were measured by heat flux DSC (from RT to 723 K), and high-temperature calorimeter (up to 1115 K) as shown in Figure S9. The combined heat capacities from 298 to 1115 K were plotted and provided in Figure 10 and the values are tabulated in Tables S6–S9. The heat capacity values were fitted in their standard function of $T(C_{p,m}^{\circ}(T) = A + BT + C/T^2)$ within a definite temperature range and are given in Table 2.

From the heat capacity data, it was observed that the $\text{NaEuCa}_8(\text{PO}_4)_6\text{F}_2$ solid solution showed lower heat capacity values as compared to other compositions. The heat capacity values obtained for Sm^{3+} and Gd^{3+} substituted compounds show higher values at high temperatures as compared to $\text{Ca}_{10}(\text{PO}_4)_6\text{F}_2$. Also, it needs to be mentioned that the heat capacity values do not show any systematic trends which

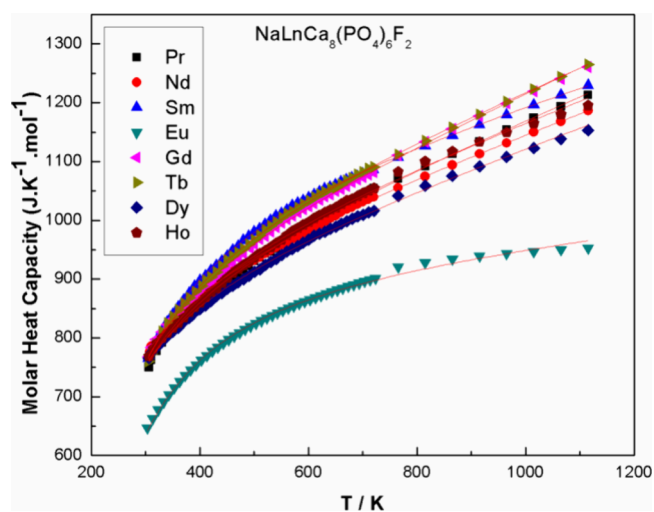


Figure 10. Heat capacities data of $\text{NaLnCa}_8(\text{PO}_4)_6\text{F}_2$ solid solutions.

Table 2. Combined Heat Capacity Expression of $\text{NaLnCa}_8(\text{PO}_4)_6\text{F}_2$ Solid Solutions (Pr–Ho Except Pm)

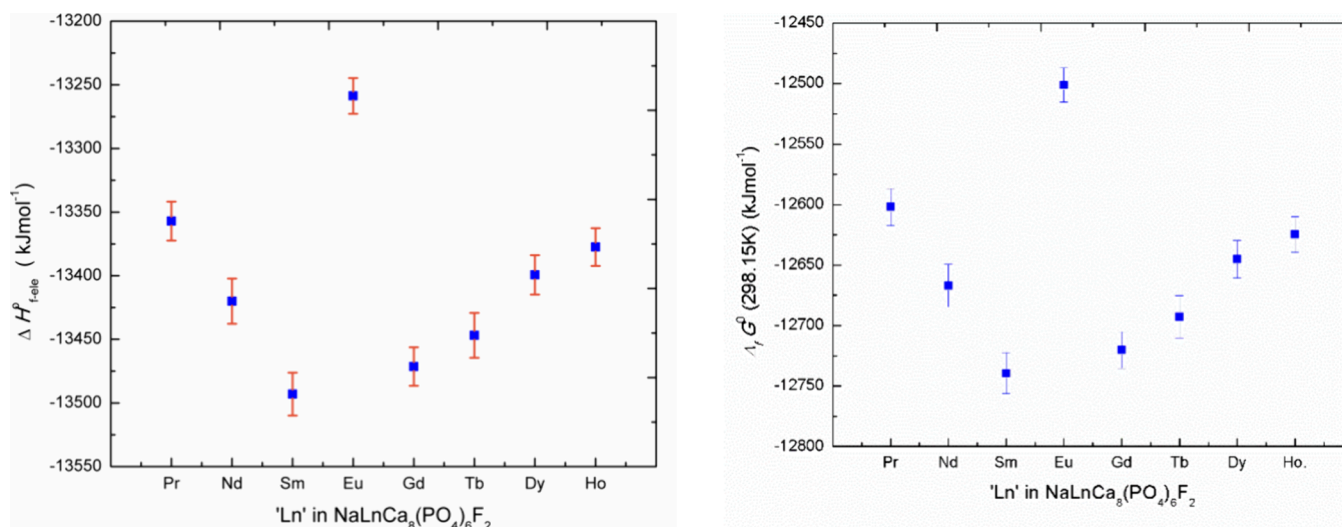
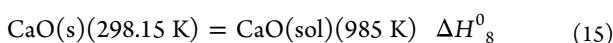
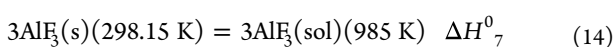
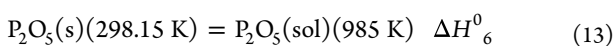
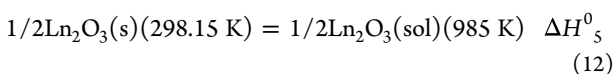
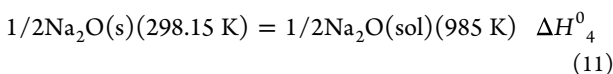
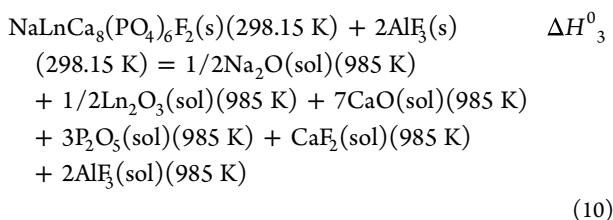
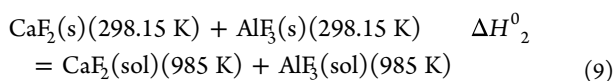
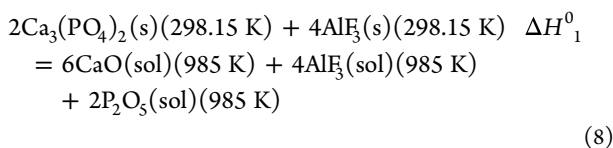
solid solutions	molar heat capacity ($\text{J mol}^{-1} \text{ K}^{-1}$) ($298 \text{ K} < T < 1115 \text{ K}$) combined $C_{p,m}^{\circ} \pm \text{SD} = A + B \times (T/\text{K}) - C/(T/\text{K})^2$
$\text{NaPrCa}_8(\text{PO}_4)_6\text{F}_2$	$C_{p,m}^{\circ} \pm 3 = 799 + 0.385 \times (T/\text{K}) - 1.48134 \times 10^7 / (T/\text{K})^2$
$\text{NaNdCa}_8(\text{PO}_4)_6\text{F}_2$	$C_{p,m}^{\circ} \pm 3 = 817 + 0.341 \times (T/\text{K}) - 1.3108 \times 10^7 / (T/\text{K})^2$
$\text{NaSmCa}_8(\text{PO}_4)_6\text{F}_2$	$C_{p,m}^{\circ} \pm 3 = 932 + 0.283 \times (T/\text{K}) - 2.34101 \times 10^7 / (T/\text{K})^2$
$\text{NaEuCa}_8(\text{PO}_4)_6\text{F}_2$	$C_{p,m}^{\circ} \pm 5 = 867 + 0.105 \times (T/\text{K}) - 2.3563 \times 10^7 / (T/\text{K})^2$
$\text{NaGdCa}_8(\text{PO}_4)_6\text{F}_2$	$C_{p,m}^{\circ} \pm 4 = 819 + 0.412 \times (T/\text{K}) - 1.63243 \times 10^7 / (T/\text{K})^2$
$\text{NaTbCa}_8(\text{PO}_4)_6\text{F}_2$	$C_{p,m}^{\circ} \pm 3 = 854 + 0.382 \times (T/\text{K}) - 1.90042 \times 10^7 / (T/\text{K})^2$
$\text{NaDyCa}_8(\text{PO}_4)_6\text{F}_2$	$C_{p,m}^{\circ} \pm 4 = 801 + 0.333 \times (T/\text{K}) - 1.30773 \times 10^7 / (T/\text{K})^2$
$\text{NaHoCa}_8(\text{PO}_4)_6\text{F}_2$	$C_{p,m}^{\circ} \pm 6 = 829 + 0.352 \times (T/\text{K}) - 1.64368 \times 10^7 / (T/\text{K})^2$

indicates that the compounds are not ideal solid solutions.²⁵ The lattice distortions play an important role in phonon propagation in the lattice structure due to asymmetry created by multiple cationic distributions of Ca^{2+} , Na^+ , and Ln^{3+} . The different Ln^{3+} occupancies play an important role in lattice asymmetry, which induces anisotropic nature in the crystals. The different occupancy distribution creates highly anisotropic crystal momentum distribution, and it has a direct influence on nonsystematic heat capacity variation.²⁵ However, it can be mentioned from the heat capacity curves as well as from thermal expansion measurements (vide supra) that the compounds do not show any phase transition up to 1115 K temperature.

For the measurement of enthalpy of formation, all these samples were mixed with AlF_3 in a 1:2 molar ratio to dissolve in $(2\text{PbO}:\text{B}_2\text{O}_3)$ solvent at 985 K and the corresponding enthalpies of dissolution were measured. The general thermochemical cycle used in this study is given in eqs 8–15.

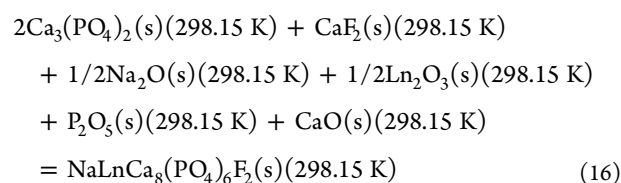
Table 3. Thermodynamic Parameters of NaLnCa₈(PO₄)₆F₂ Solid Solutions Obtained at Ambient Temperature

solid solutions	$\Delta_f H^0$ (298.15 K) (kJ mol ⁻¹)	$\Delta_f S^0$ (298.15 K) (J mol ⁻¹ K ⁻¹)	$\Delta_f G^0$ (298.15 K) (kJ mol ⁻¹)
NaPrCa ₈ (PO ₄) ₆ F ₂	-13357.1 ± 15.3	-2534	-12602.0 ± 15.3
NaNdCa ₈ (PO ₄) ₆ F ₂	-13420.0 ± 17.8	-2527	-12667.0 ± 17.8
NaSmCa ₈ (PO ₄) ₆ F ₂	-13493.0 ± 16.9	-2529	-12739.4 ± 16.9
NaEuCa ₈ (PO ₄) ₆ F ₂	-13258.7 ± 14.1	-2542	-12501.2 ± 14.1
NaGdCa ₈ (PO ₄) ₆ F ₂	-13471.4 ± 15.1	-2521	-12720.2 ± 15.1
NaTbCa ₈ (PO ₄) ₆ F ₂	-13446.8 ± 17.7	-2530	-12692.9 ± 17.7
NaDyCa ₈ (PO ₄) ₆ F ₂	-13399.3 ± 15.5	-2531	-12645.1 ± 15.5
NaHoCa ₈ (PO ₄) ₆ F ₂	-13377.4 ± 14.8	-2526	-12624.7 ± 14.8

**Figure 11.** Enthalpy of formation and Gibbs free energy of formation values of NaLnCa₈(PO₄)₆F₂ solid solutions at 298.15 K.

For simplification, all the equations corresponding to observed enthalpies of dissolution were expressed as the sum

of the total enthalpy increments from 298.15 to 985 K and the enthalpy of solutions (985 K). The detailed analyzed data of enthalpies of dissolution are provided in Table S10. ΔH^0_1 (985 K), ΔH^0_2 (985 K), ΔH^0_4 (985 K), ΔH^0_5 (985 K), ΔH^0_6 (985 K), ΔH^0_7 (985 K), ΔH^0_8 (985 K) values of eqs 8, 9, and 11–15 were taken from literature.^{35,50–54} Eq 12 is represented as a general equation for all the lanthanides used in the present study. The enthalpy of dissolution values of Pr₂O₃ and Tb₂O₃ were calculated at 985 K from experimental solution data obtained at 1073 K.^{50–53} Since there is hardly any difference obtained in enthalpy of solution values at 977 and 1073 K as previously proved experimentally by Zhang et al.,⁵³ corresponding heat of solutions values of Pr₂O₃ and Tb₂O₃ at 1073 K were coupled with enthalpy increment values to calculate the total enthalpy of dissolution of Pr₂O₃ and Tb₂O₃ at 985 K.^{50–53} The ΔH^0_3 (985 K) values for eq 10 of NaLnCa₈(PO₄)₆F₂(s) solid solutions were experimentally measured in the present study. Finally, by using a thermochemical cycle ($\Delta H^0_1 + \Delta H^0_2 - \Delta H^0_3 + \Delta H^0_4 + \Delta H^0_5 + \Delta H^0_6 - \Delta H^0_7 + \Delta H^0_8$) shown above, we obtained $\Delta_f H^0$ (298.15 K) of the following eq 16:



From Hess's law, $\Delta_f H^0$ (298.15 K) of eq 13 is related to $\Delta_f H^0$ (298.15 K) of the product and reactant by eq 17.⁵⁵

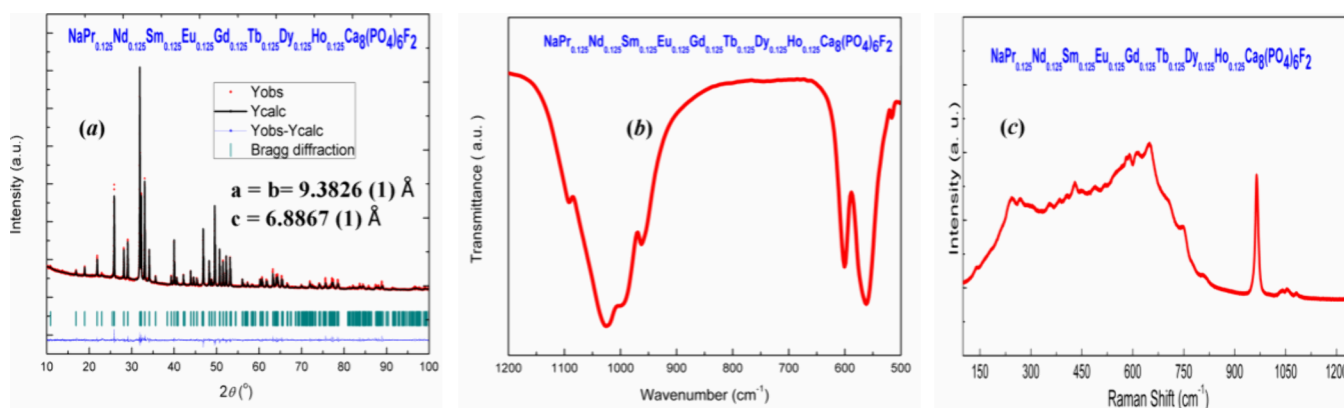
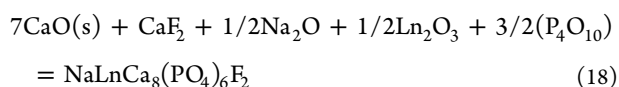


Figure 12. (a) XRD, (b) FTIR and (c) Raman spectra of WF-Ln.

$$\begin{aligned} \Delta_f H^0(298.15 \text{ K}) &= \Delta_f H^0(298.15 \text{ K})(\text{NaLnCa}_8(\text{PO}_4)_6\text{F}_2, \text{ s}) \\ &- 2\Delta_f H^0(298.15 \text{ K})(\text{Ca}_3(\text{PO}_4)_2, \text{ s}) - \Delta_f H^0(298.15 \text{ K}) \\ &(\text{CaF}_2, \text{ s}) - 1/2\Delta_f H^0(298.15 \text{ K})(\text{Na}_2\text{O}, \text{ s}) \\ &- 1/2\Delta_f H^0(298.15 \text{ K})(\text{Ln}_2\text{O}_3, \text{ s}) - \Delta_f H^0(298.15 \text{ K}) \\ &(\text{P}_2\text{O}_5, \text{ s}) - \Delta_f H^0(298.15 \text{ K})(\text{CaO}, \text{ s}) \end{aligned} \quad (17)$$

Now, enthalpy of formation values except that of $\text{NaLnCa}_8(\text{PO}_4)_6\text{F}_2$ solid solutions are taken from the literature⁵⁴ to calculate $\Delta_f H^0(298.15 \text{ K})(\text{NaLnCa}_8(\text{PO}_4)_6\text{F}_2, \text{ s})$ solid solutions using eq 17. The obtained $\Delta_f H^0(298.15 \text{ K})$ values are provided in Table 3 and shown as a function of Ln^{3+} in Figure 11. It was observed that the enthalpy of formation value of $\text{NaEuCa}_8(\text{PO}_4)_6\text{F}_2$ solid solution was lower as compared to other lanthanide-substituted CaFAp analogues. The plausible reason might be due to significantly less enthalpy of formation value of Eu_2O_3 i.e., $-1651.4 \text{ kJ mol}^{-1}$ compared to other lanthanide oxides.⁵⁴ The standard state of europium is a divalent state due to a half-filled $4f^7$ electronic configuration. Hence, an additional amount of energy must be absorbed to convert divalent europium to its trivalent state.

We have calculated $\Delta_f S^0(298.15 \text{ K})$ of these solid solutions from the absolute entropy from corresponding solid lattice contribution parts and configuration entropy calculation by cationic occupancies obtained from Rietveld refinement studies. For absolute lattice entropy estimation, we assumed an empirical equation for the formation of the compounds from their corresponding oxides and fluorides according to eq 18.^{54,56}



However, we need to add the configurational entropy $S^0(0 \text{ K})$ part into these values to get total absolute entropy values, since these are solid solutions. To calculate configurational entropy values we have considered the cationic occupancy values obtained from our structural studies and used Sterling approximation to calculate $S^0(0 \text{ K})$ values of the compounds.⁵⁵ After adding these $S^0(0 \text{ K})$ values, we have calculated $S^0(298.15 \text{ K})$ with an assumption that entropy contributions such as electronic, magnetic, and Schottky were negligible as compared to lattice contribution using eq 19.

$$S^0(298.15 \text{ K}) = S^0(0 \text{ K}) (\text{configurational}) + S^0(298.15 \text{ K}) (\text{lattice}) \quad (19)$$

From these $S^0(298.15 \text{ K})$ values, we have calculated $\Delta_f S^0(298.15 \text{ K})$ of the compounds by subtracting the $S^0(298.15 \text{ K})$ values of the constituting elements, and the values are provided in Table 3 and shown in Figure S10. From the values of $\Delta_f H^0(298.15 \text{ K})$ and $\Delta_f S^0(298.15 \text{ K})$, we calculated $\Delta_f G^0(298.15 \text{ K})$ of the compounds as shown in Figure 11. It is clear that Sm^{3+} and Gd^{3+} substituted CaFAp are having higher formation enthalpy $\Delta_f H^0(298.15 \text{ K})$ which in turn gives rise to the higher free energy of formation $\Delta_f G^0(298.15 \text{ K})$ as the entropy term does not contribute much. This stability of Sm^{3+} and Gd^{3+} substituted CaFAp might be due to similar ionic radii of Sm^{3+} , Gd^{3+} , and Ca^{2+} (1.02, 1.00, and 1.06 Å, respectively) in seven coordination.

Multilanthanide-Doped CaFAp. From the above discussion, it is clear that charge-coupled substitution of Na^+ and Ln^{3+} in CaFAp up to 10 at % does not produce any adverse effect in terms of phase, thermal, as well as thermodynamic stability. Hence, we synthesized multiple lanthanides substituted CaFAp to study the effect of multiple lanthanides loading at once in the CaFAp matrix. The total lanthanides substitution was kept at 10 at %. The composition of the synthesized compound was $\text{NaPr}_{0.125}\text{Nd}_{0.125}\text{Sm}_{0.125}\text{Eu}_{0.125}\text{Gd}_{0.125}\text{Tb}_{0.125}\text{Dy}_{0.125}\text{Ho}_{0.125}\text{Ca}_8(\text{PO}_4)_6\text{F}_2$ (WF-Ln). The optimized synthesized condition is shown in Figure S11 by taking XRD patterns at various temperatures. The XRD pattern after the Rietveld refinement is shown in Figure 12a. XRD shows that the pure phase of fluorapatite was formed without any impurity for this composition. The refinement was carried out by keeping the occupancy of all lanthanides the same at the Ca1 and Ca2 sites. After refinement, the occupancy values at Ca1 and Ca2 sites are 18% and 82%, respectively. The lattice parameters obtained by Rietveld refinement ($a = 9.3826(1) \text{ \AA}$ and $c = 6.8867(1) \text{ \AA}$) are in a close match with the single Ln substituted CaFAp compositions. Figure S12 displays the elemental mapping of this multilanthanide(WF-Ln) solid solution. EDS concentration analysis was conducted on four distinct zones, as depicted in Figure S13. For all recorded EDS, the X-ray peaks of the lanthanides merged together, making it challenging to accurately determine the compositions of multiple lanthanides in different grains of the sample (Figure S13). Nevertheless, the elemental mapping obtained for a larger zone in Figure S12 supports the micro-homogeneous nature of the sample.

IR and Raman investigations (Figure 12b,c) of WF-Ln show that the local structure is similar to the single lanthanide-doped CaFap as no extra peaks are observed in FTIR and Raman spectra. These structural studies confirm the incorporation of multilanthanides in CaFap forming a single phase. The volume thermal expansivity of WF-Ln is calculated from HTXRD and found to be $36.2 \times 10^{-6}/\text{K}$. This value is larger than the additive value of α_v ($33.4 \times 10^{-6}/\text{K}$) obtained from mono lanthanide substituted CaFap compositions. This observation is in compliance with the cocktail effect coined for multi-elemental doping in high entropy oxides. This effect states that some excess value in thermal properties is added due to the significant lattice distortion arising from multi-element substitution.⁵⁷ The expressions for heat capacity obtained from DSC, enthalpy increment data, as well as combined heat capacity data obtained from DSC and enthalpy increment are given in Table 4 and provided in Figure S14. The enthalpy of

Table 4. Expressions for Heat Capacity Obtained from DSC, Enthalpy Increment Data, as Well as Combined Heat Capacity Obtained from DSC and Enthalpy Increment of Multilanthanide (WF-Ln) Solid Solution

thermodynamic parameters	experimentally determined expressions
$C_{p,m}^{\circ}(T)$ from DSC (298 K < T < 720 K)	$C_{p,m}^{\circ}(T) \pm 2 = 793 + 0.368 \times (T/\text{K}) - 1.26822 \times 10^7/(T/\text{K})^2$
enthalpy increment (298 K < T < 1115 K)	enthalpy increment $\pm 5841 = -301461 + 804 \times (T/\text{K}) + 0.182 \times (T/\text{K})^2 - 1.37378 \times 10^7/(T/\text{K})$
combined $C_{p,m}^{\circ}(T)$ from DSC and enthalpy increment (298 K < T < 1115 K)	$C_{p,m}^{\circ}(T) \pm 3 = 789 + 0.376 \times (T/\text{K}) - 1.25657 \times 10^7/(T/\text{K})^2$

formation was experimentally measured as -13393.1 ± 16.8 kJ mol⁻¹. The calculated entropy of the formation value was obtained as -2434 J mol⁻¹ K⁻¹. The obtained values of formation enthalpy and entropy were used to calculate mixing enthalpy and entropy contribution as compared to additive enthalpy and entropy of formation values of singly lanthanide-doped compounds based on eqs 20 and 21.

$$\Delta H_{\text{mix}}(298.15 \text{ K}) = \Delta_f H^{\circ}(298.15 \text{ K})(\text{WF-Ln}) - 0.125 \times [\Sigma \Delta_f H^{\circ}(298.15 \text{ K})(\text{NaLnCa}_8(\text{PO}_4)_6\text{F}_2)] \quad (20)$$

$$\Delta S_{\text{mix}}(298.15 \text{ K}) = \Delta_f S^{\circ}(298.15 \text{ K})(\text{WF-Ln}) - 0.125 \times [\Sigma \Delta_f S^{\circ}(298.15 \text{ K})(\text{NaLnCa}_8(\text{PO}_4)_6\text{F}_2)] \quad (21)$$

The calculated ΔH_{mix} value was obtained as 9.867 ± 0.04 kJ mol⁻¹ which shows unfavorable endothermic mixing. However, even at room temperature the $T\Delta S_{\text{mix}}$ term predominates over ΔH_{mix} value due to the high configuration entropy contribution of the multilanthanide apatite system and makes the overall negative ΔG_{mix} value as -18.742 ± 0.04 kJ mol⁻¹ at 298.15 K. This implies that entropy is the main driving force to stabilize the multilanthanide substitution in fluorapatite.

Effect of Electron Irradiation on Fluorapatite Waste Forms. To ensure the β^- radiation stability of synthesized ceramic waste forms, Ln³⁺ substituted CaFap compounds were irradiated with an electron beam with 1 and 20 MGy irradiation doses. After the irradiation, powder XRD patterns of solid solutions were recorded and are shown in Figures S15 and S16 (magnified view). XRD patterns do not show any sign of phase decomposition and phase transformation after irradiation up to 20 MGy as no new peaks are observed in the XRD patterns. The crystallinity of the irradiated compounds was modified upon irradiation as observed from the calculated fwhm values of [002] planes of irradiated NaLnCa₈(PO₄)₆F₂ solid solutions given in Figure S17. As a general trend, observed for 1 MGy irradiated samples, the peak intensity was enhanced as compared to unirradiated samples while for 20 MGy dose, the intensity of XRD peaks became poorer. At low-dose electron irradiation, it was reported that crystallinity increased in the case of britholite, apatite, and zircon.^{58–60} This crystallization effect was either due to the temperature increase during electron irradiation or by the ionizing effect of the electron beam. This observation confirmed that Ln³⁺ substituted CaFap waste forms were

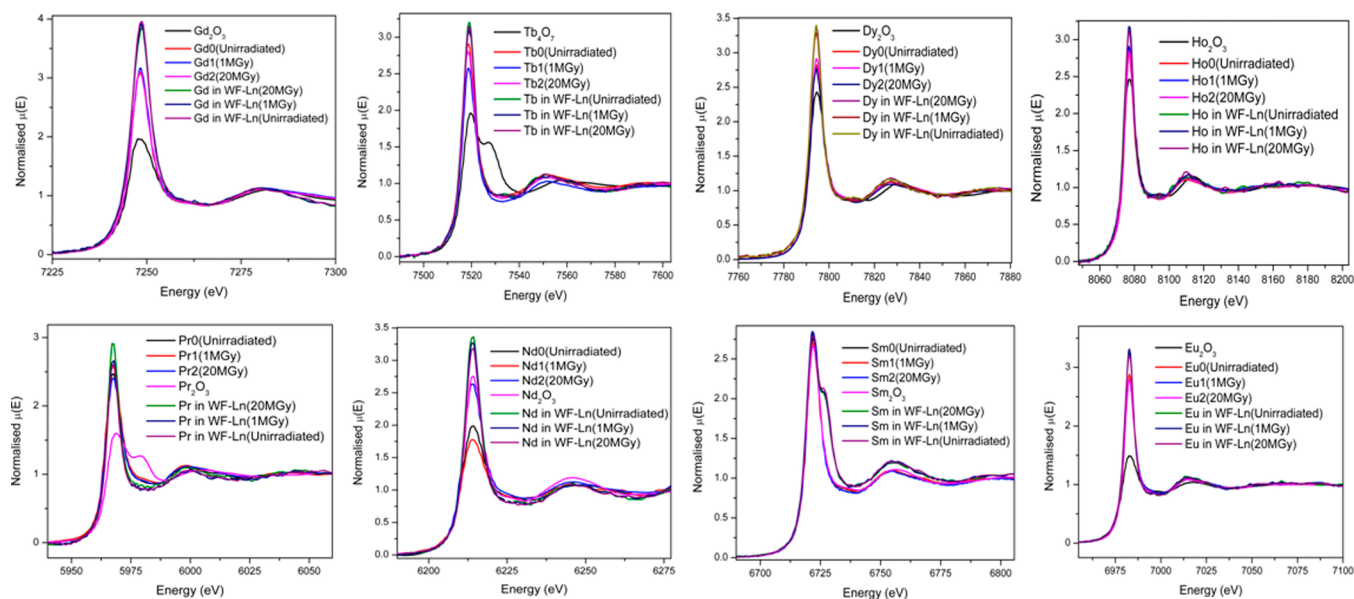


Figure 13. Normalized XANES spectra at rare earth L3-edge along with respective standards.

highly β^- radiation-resistant with respect to the actual phase. To get more insight into the local structural changes of these irradiated samples, FTIR and Raman spectra were recorded (Figures S18 and S19). These spectra show no changes with respect to those of unirradiated samples. Earlier, we reported the radiation stability of CaFAP against β^- radiation up to 1 MGy and there were no observable changes in phase as well as local structure. The unaltered nature of FTIR and Raman spectra clearly indicates that these waste forms certainly do not decompose or transform in other phases.

To get further insight into the effect of irradiation on the local structure at Ln sites, we carried out XANES and EXAFS studies at the L_3 edge of substituted lanthanide ions. The normalized XANES spectra, along with their respective standards, are shown in Figure 13. All spectra displayed the characteristic white line (L_3 edge), which is a prominent absorption resonance positioned at the absorption edge. This phenomenon arises from the electric-dipole allowed ($\Delta l = \pm 1$) transition from the core state $2p_{3/2}$ to quasi-bound states with atomic character $5d$ of lanthanides.⁶¹ It is clear from the figure that all of the lanthanides exist in +3 standard oxidation states before and after irradiation. There are small deviations in the white line intensity of unirradiated and irradiated samples, which signifies that there is some distortion in the coordination environment of lanthanides in single lanthanide substitution. However, in multilanthanide-doped samples, the white line intensity of different Ln absorption edges is higher as compared to the single lanthanide-doped sample. Moreover, there is no change in the absorption edge intensities at all lanthanide edges even after a 20 MGy dose of electron beam-induced irradiation. This observation might be due to severe lattice distortion and compositional complexity in the lattice structure. Hence, this lattice distortion contributes to the higher kinetic barrier for irradiation-induced effects aggregation to form defect clusters and voids.^{62–65} This observation also points out that WF-Ln is not affected by electron irradiation. A distinct shoulder was observed for WF-Ln at the Sm L_3 edge whereas there is only one peak for Sm-doped samples. The presence of a doublet is due to the close proximity of Ho L_2 edge ($\Delta E = 6$ eV).

Local structural information was extracted by analyzing the EXAFS region of the absorption spectra. The $\chi(R)$ versus R plots, derived from the Fourier transform of $\chi(k)$ spectra, are illustrated in Figure 14 at the rare earth L_3 -edges. The EXAFS analysis of the mixed doped sample could not be performed due to the presence of various absorption peaks from other rare earth elements immediately after the L_3 absorption edge. The displayed Fourier transform spectra are not phase-corrected, leading to the coordination peak in these spectra appearing at slightly lower interatomic distances (R) in comparison to the actual bond length. To simulate the theoretical EXAFS spectrum, structural parameters were obtained from XRD results. The XAS analysis was conducted using the Demeter package, incorporating ATHENA and ARTEMIS subroutines for data processing and analysis.⁶⁶ Fitting parameters, such as bond length, coordination number, and disorder factor (σ^2), were varied for analysis. The outcomes of the fitting process are presented in Table S11, and the optimal fitting spectra are illustrated in Figure 14a–h. The Fourier transformation of EXAFS spectra shows a first near-neighbor peak around 1.85 Å and two next near-neighbor peaks around 3.0 and 3.8 Å. The first peak is the contribution of three scattering paths one from fluorine and two from

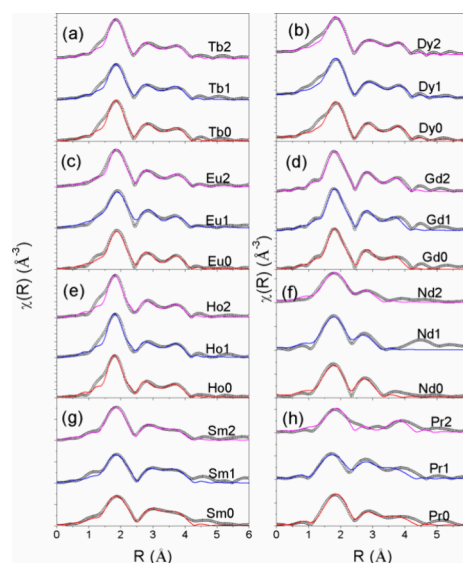


Figure 14. Fourier-transform EXAFS spectrum (scatter points) and the respective fittings (solid line) of unirradiated (labeled as 0), 1 MGy irradiated (labeled as 1), and 20 MGy irradiated (labeled as 2) at rare-earth L_3 -edges; (a) NaTbCa₈(PO₄)₆F₂ samples, (b) NaDyCa₈(PO₄)₆F₂ samples, (c) NaEuCa₈(PO₄)₆F₂ samples, (d) NaGdCa₈(PO₄)₆F₂ samples, (e) NaHoCa₈(PO₄)₆F₂ samples, (f) NaNdCa₈(PO₄)₆F₂ samples, (g) NaSmCa₈(PO₄)₆F₂ samples, (h) NaPrCa₈(PO₄)₆F₂ samples. The spectra are vertically shifted for a better illustration.

oxygen scattering paths around 2.31, 2.36, and 2.53 Å, respectively. The obtained bond lengths from EXAFS analysis indicate average coordination around the absorbing atom which is in good agreement with the XRD data. The average coordination number observed for the first coordination peak exceeds 7 across all absorption edges. This suggests the presence of rare earths at two crystallographic sites, namely, seven coordinated and nine coordinated. The average bond lengths and coordination numbers depicted in Table S11 indicate a similar coordination environment around all the rare earths even after the irradiation. Hence, the XANES and EXAFS data corroborated that Ln substitutes CaFAPs are radiation resistant with respect to oxidation state and local structure modification.

With this study, we confirm that upon charge coupled substitution with Na⁺ and Ln³⁺ in CaFAP up to 10 atom %, the β^- radiation stability of CaFAP ceramic waste forms does not deteriorate. However, in the case of multilanthanide-substituted WF-Ln, there was hardly any change observed in XRD, FTIR, and Raman studies, as shown in Figure S20.

CONCLUSIONS

Charge-coupled substitution in calcium fluorapatite (CaFAP) with a composition of NaLnCa₈(PO₄)₆F₂ (Ln = La to Lu) was successfully achieved. These compositions are structurally characterized and show a similar structure to that of CaFAP. Thermophysical properties such as thermal expansion and heat capacities of these solid solutions correspond to the model waste form CaFAP and Ln substitution does not alter these characteristics. Thermodynamic stability is marked by a similar formation enthalpy as that of CaFAP. Multilanthanides are successfully substituted as a single-phase matrix with the formula NaPr_{0.125}Nd_{0.125}Sm_{0.125}Eu_{0.125}Gd_{0.125}Tb_{0.125}Dy_{0.125}Ho_{0.125}Ca₈(PO₄)₆F₂ for the first time. This

composition has been shown to be entropy stabilized at room temperature, supported by thermodynamic studies. Electron beam irradiation studies, supported by XRD, FTIR, Raman, and X-ray absorption measurements, demonstrate that fluorapatites are radiation-resistant waste forms. These structural, thermodynamic, and radiation stability studies clearly present CaFAP as a model waste form for fluoride-containing radioactive waste.

■ ASSOCIATED CONTENT

SI Supporting Information

The Supporting Information is available free of charge at <https://pubs.acs.org/doi/10.1021/acsomega.4c04809>.

Figures and tables related to the experiments in this study (PDF)

■ AUTHOR INFORMATION

Corresponding Authors

Pratik Das – Product Development Division, Bhabha Atomic Research Centre, Mumbai 400085, India; Homi Bhabha National Institute (HBNI), Mumbai 400094, India; Email: pratikdas@barc.gov.in

Bal Govind Vats – Fuel Chemistry Division, Bhabha Atomic Research Centre, Mumbai 400085, India; Homi Bhabha National Institute (HBNI), Mumbai 400094, India; orcid.org/0000-0002-4936-6957; Email: bgvats@barc.gov.in

Suresh Chandra Parida – Product Development Division, Bhabha Atomic Research Centre, Mumbai 400085, India; Homi Bhabha National Institute (HBNI), Mumbai 400094, India; Email: sureshp@barc.gov.in

Authors

Pradeep Samui – Product Development Division, Bhabha Atomic Research Centre, Mumbai 400085, India; Homi Bhabha National Institute (HBNI), Mumbai 400094, India

Abhishek Kumar Rai – Product Development Division, Bhabha Atomic Research Centre, Mumbai 400085, India; Homi Bhabha National Institute (HBNI), Mumbai 400094, India

Ashok Kumar Yadav – Atomic & Molecular Physics Division, Bhabha Atomic Research Centre, Mumbai 400085, India; Homi Bhabha National Institute (HBNI), Mumbai 400094, India; orcid.org/0000-0003-2716-0971

Muhammed Shafeeq – Fuel Chemistry Division, Bhabha Atomic Research Centre, Mumbai 400085, India

Swayam Kesari – Solid State Physics Division, Bhabha Atomic Research Centre, Mumbai 400085, India

Complete contact information is available at: <https://pubs.acs.org/doi/10.1021/acsomega.4c04809>

Author Contributions

P.D.: Conceptualization, Methodology, Visualization, Planning, Synthesis, XRD study, Rietveld refinement and analysis, writing the manuscript. B.G.V.: Conceptualization, Synthesis, Rietveld refinement, IR study, HTXRD study, interpretation of the results, writing and editing of the final draft, P.S. and A.K.R.: Thermodynamic studies, A.K.Y.: XAS spectroscopic analysis and writing, M.S.: HTXRD experiment, S.K.: Raman experiments and S.C.P.: Visualization, Supervising, Correction of the final draft, Conceptualization.

Notes

The authors declare no competing financial interest.

■ ACKNOWLEDGMENTS

The authors are thankful to Dr. P. K. Mohapatra, Group Director, Radiochemistry and Isotope Group, BARC, Mumbai for his encouragement, motivation, and constant support throughout this work. Authors also acknowledge Dr. Archana Sharma (Director, BTDG, BARC), Shri R. B. Chavan and Shri Mukesh Kumar (APPD, BARC) for their help in the Electron Beam experiment at EBC Kharghar. The authors would also like to acknowledge Dr. R. R. Urkude and Dr. Biplab Ghosh (BDAS, BARC, Mumbai) for carrying out the XAS experiment at BL-09, Indus-2, RRCAT, Indore.

■ REFERENCES

- (1) Yoshioka, R. Nuclear energy based on thorium molten salt. In *Molten Salts Chemistry*; Elsevier: 2013; pp 471–496.
- (2) Delpech, S. Molten salts for nuclear applications. In *Molten Salts Chemistry*; Elsevier: 2013; pp 497–520.
- (3) Serp, J.; Allibert, M.; Beneš, O.; Delpech, S.; Feynberg, O.; Ghetta, V.; Heuer, D.; Holcomb, D.; Ignatiev, V.; Kloosterman, J. L.; et al. The molten salt reactor (MSR) in generation IV: overview and perspectives. *Prog. Nucl. Energy* **2014**, *77*, 308–319.
- (4) Baes, C., Jr The chemistry and thermodynamics of molten salt reactor fuels. *J. Nucl. Mater.* **1974**, *51* (1), 149–162.
- (5) Li, W.; Li, Q. Molten salt reactor: a new source of innovation development for radiochemistry. *J. Nucl. Radiochem.* **2016**, *38* (6), 327–336.
- (6) Srivastava, A. K.; Chouhan, R.; Borgohain, A.; Jana, S. S.; Maheshwari, N. K.; Pilkhal, D. S.; Rama Rao, A.; Hareendhran, K. N.; Chowdhury, S.; Modi, K. B.; et al. An Experimental and Numerical Study to Support Development of Molten Salt Breeder Reactor. *J. Nucl. Eng. Radiat. Sci.* **2017**, *3* (3), No. 031007.
- (7) Compere, E.; Kirslis, S.; Bohlmann, E.; Blankenship, F.; Grimes, W. *Fission product behavior in the molten salt reactor experiment*; Oak Ridge National Lab.(ORNL): Oak Ridge, TN (United States), 1975.
- (8) Riley, B. J.; McFarlane, J.; DelCul, G. D.; Vienna, J. D.; Contescu, C. I.; Forsberg, C. W. Molten salt reactor waste and effluent management strategies: A review. *Nucl. Eng. Des.* **2019**, *345*, 94–109.
- (9) Singh, B. K.; Hafeez, M. A.; Kim, H.; Hong, S.; Kang, J.; Um, W. Inorganic waste forms for efficient immobilization of radionuclides. *ACS ES&T Engineering* **2021**, *1* (8), 1149–1170.
- (10) Ojovan, M. I.; Lee, W. E. Glassy wasteforms for nuclear waste immobilization. *Metallurgical and Materials Transactions A* **2011**, *42*, 837–851.
- (11) Lukens, W. W.; Magnani, N.; Tyliczszak, T.; Pearce, C. I.; Shuh, D. K. Incorporation of technetium into spinel ferrites. *Environ. Sci. Technol.* **2016**, *50* (23), 13160–13168.
- (12) Vats, B. G.; Rawat, D.; Shafeeq, M.; Shelke, G. P.; Keskar, M.; Krishnan, K. Ternary U (IV) containing phosphates: synthesis, structure and thermodynamic studies. *J. Alloys Compd.* **2019**, *798*, 174–186.
- (13) Donald, I.; Metcalfe, B.; Taylor, R. J. The immobilization of high level radioactive wastes using ceramics and glasses. *J. Mater. Sci.* **1997**, *32* (22), 5851–5887.
- (14) Zarzycki, J. *Glasses and the vitreous state*; Cambridge University Press: 1991.
- (15) McCarthy, G. J.; White, W. B.; Roy, R.; Scheetz, B. E.; Komarneni, S.; Smith, D. K.; Roy, D. M. Interactions between nuclear waste and surrounding rock. *Nature* **1978**, *273* (5659), 216–217.
- (16) McCarthy, G. J. High-level waste ceramics: materials considerations, process simulation, and product characterization. *Nuclear Technology* **1977**, *32* (1), 92–105.

- (17) Mandal, B. P.; Pandey, M.; Tyagi, A. K. Gd₂Zr₂O₇ pyrochlore: Potential host matrix for some constituents of thorium based reactor's waste. *J. Nucl. Mater.* **2010**, *406* (2), 238–243.
- (18) Ringwood, A. E.; Kesson, S. E.; Ware, N. G.; Hibberson, W.; Major, A. Immobilisation of high level nuclear reactor wastes in SYNROC. *Nature* **1979**, *278* (5701), 219–223.
- (19) Loiseau, P.; Caurant, D.; Majerus, O.; Baffier, N.; Fillet, C. Crystallization study of (TiO₂, ZrO₂)-rich SiO₂-Al₂O₃-CaO glasses Part II Surface and internal crystallization processes investigated by differential thermal analysis (DTA). *J. Mater. Sci.* **2003**, *38*, 853–864.
- (20) Caurant, D.; Majerus, O.; Loiseau, P.; Bardez, I.; Baffier, N.; Dussossoy, J. Crystallization of neodymium-rich phases in silicate glasses developed for nuclear waste immobilization. *J. Nucl. Mater.* **2006**, *354* (1–3), 143–162.
- (21) Ojovan, M. I.; Yudin, S. V. Glass, ceramic, and glass-crystalline matrices for HLW immobilisation. *Open Ceramics* **2023**, *14*, No. 100355.
- (22) Garcia-Sanchez, T.; Diaz-Anichtchenko, D.; Muñoz, A.; Rodriguez-Hernandez, P.; Marqueño, T.; Jafar, M.; Achary, S. N.; Alabarse, F.; Errandonea, D. High-Pressure X-ray Diffraction Study of Orthorhombic Ca₂Zr₅Ti₂O₁₆. *J. Phys. Chem. C* **2023**, *127* (4), 2069–2077.
- (23) Errandonea, D.; Turnbull, R.; Sánchez-Martín, J.; Oliva, R.; Muñoz, A.; Radescu, S.; Mujica, A.; Blackburn, L.; Hyatt, N. C.; Popescu, C.; Ibáñez-Insa, J. A comparative study of the high-pressure structural stability of zirconolite materials for nuclear waste immobilisation. *Results in Physics* **2024**, *61*, No. 107704.
- (24) Das, P.; Vats, B. G.; Samui, P.; Kesari, S.; Shafeeq, M.; Parida, S. C.; Dash, S. Exploring the Thermodynamic Behavior and the Effect of Temperature and Electron Radiation on the Structure of Fluorapatite Compounds. *ChemistrySelect* **2021**, *6* (48), 13817–13831.
- (25) Das, P.; Vats, B. G.; Shafeeq, M.; Samui, P.; Kesari, S.; Parida, S. Studies on the variation of structural and thermodynamic properties of charge coupled substituted Na_xEu_xCa_{10-2x}(PO₄)₆F₂ solid solutions (x = 0.5–2.0). *J. Alloys Compd.* **2022**, *923*, No. 166331.
- (26) Das, P.; Pathak, N.; Modak, P.; Modak, B. Multifunctional Ca₁₀(PO₄)₆F₂ as a host for radioactive waste immobilization: Am³⁺/Eu³⁺ ions distribution, phosphor characteristics and radiation induced changes. *Journal of Hazardous Materials* **2021**, *411*, No. 125025.
- (27) Zhang, X.; Zhang, J.; Huang, J.; Tang, X.; Gong, M. Synthesis and luminescence of Eu²⁺-doped alkaline-earth apatites for application in white LED. *Journal of Luminescence* **2010**, *130* (4), 554–559.
- (28) Zeng, Q.; Liang, H.; Zhang, G.; Birowosuto, M. D.; Tian, Z.; Lin, H.; Fu, Y.; Dorenbos, P.; Su, Q. Luminescence of Ce³⁺ activated fluoro-apatites M₅(PO₄)₃F (M = Ca, Sr, Ba) under VUV–UV and x-ray excitation. *J. Phys.: Condens. Matter* **2006**, *18* (42), 9549.
- (29) Zawisza, K.; Sobierajska, P.; Renaudin, G.; Nedelec, J.-M.; Wiglus, R. J. Effects of crystalline growth on structural and luminescence properties of Ca (10–3x) Eu 2x (PO₄)₆F₂ nanoparticles fabricated by using a microwave driven hydrothermal process. *CrystEngComm* **2017**, *19* (46), 6936–6949.
- (30) Xia, Y.; Liu, Y.-G.; Huang, Z.; Fang, M.; Molokeev, M. S.; Mei, L. Ca₆La₄(SiO₄)₂(PO₄)₄O₂:Eu²⁺: a novel apatite green-emitting phosphor for near-ultraviolet excited w-LEDs. *Journal of Materials Chemistry C* **2016**, *4* (21), 4675–4683.
- (31) Ravikumar, R.; Gopal, B.; Jena, H. Crystal Chemical Substitution at Ca and La Sites in CaLa₄(SiO₄)₃O To Design the Composition Ca_{1-x}M_xLa_{4-x}RE_x(SiO₄)₃O for Nuclear Waste Immobilization and Its Influence on the Thermal Expansion Behavior. *Inorg. Chem.* **2018**, *57* (11), 6511–6520.
- (32) Cranswick, L. *Computer software for powder diffraction*; 2008. DOI: 10.1039/9781847558237-00494
- (33) Rodríguez-Carvajal, J. Recent advances in magnetic structure determination by neutron powder diffraction. *Physica B: Condensed Matter* **1993**, *192* (1), 55–69.
- (34) Jain, D.; Nuwad, J.; Sudarsan, V.; Tyagi, A. K. Effect of structural phase transitions on high temperature thermal conductivity of nuclear-grade uranium. *J. Alloys Compd.* **2020**, *831*, No. 154706.
- (35) Westrich, H. R.; Navrotsky, A. Some thermodynamic properties of fluorapatite, fluoropargasite, and fluorphlogopite. *American journal of science* **1981**, *281* (8), 1091–1103.
- (36) Chaudhary, N.; Singh, A.; Aswal, D.; Jha, P.; Samanta, S.; Chauhan, A.; Debnath, A.; Acharya, S.; Shah, K.; Muthe, K.; et al. Electron beam induced modifications of polyaniline silver nanocomposite films: Electrical conductivity and H₂S gas sensing studies. *Radiat. Phys. Chem.* **2018**, *153*, 131–139.
- (37) Basu, S.; Nayak, C.; Yadav, A.; Agrawal, A.; Poswal, A.; Bhattacharyya, D.; Jha, S.; Sahoo, N. A comprehensive facility for EXAFS measurements at the INDUS-2 synchrotron source at RRCAT, Indore, India. In *Journal of Physics: Conference Series*; IOP Publishing: 2014; Vol. 493, p 012032.
- (38) Poswal, A.; Agrawal, A.; Yadav, A.; Nayak, C.; Basu, S.; Kane, S.; Garg, C.; Bhattacharyya, D.; Jha, S.; Sahoo, N. Commissioning and first results of scanning type EXAFS beamline (BL-09) at INDUS-2 synchrotron source. In *AIP Conference Proceedings*; American Institute of Physics: 2014; Vol. 1591, pp 649–651.
- (39) Mayer, I.; Roth, R.; Brown, W. Rare earth substituted fluoride-phosphate apatites. *J. Solid State Chem.* **1974**, *11* (1), 33–37.
- (40) Kreidler, E. R.; Hummel, F. The crystal chemistry of apatite: structure fields of fluor- and chlorapatite. *Am. Mineral.* **1970**, *55* (1–2), 170–184.
- (41) Eiberger, B.; Greenblatt, M. Rare-earth-substituted chlorophosphate apatites. *J. Solid State Chem.* **1982**, *41* (1), 44–49.
- (42) Toumi, M.; Smiri-Doggy, L.; Bulou, A. Crystal structure and polarized Raman spectra of Ca₆Sm₂Na₂(PO₄)₆F₂. *J. Solid State Chem.* **2000**, *149* (2), 308–313.
- (43) Mayer, I.; Cohen, S. The crystal structure of Ca₆Eu₂Na₂(PO₄)₆F₂. *J. Solid State Chem.* **1983**, *48* (1), 17–20.
- (44) White, T. J.; Dong, Z. Structural derivation and crystal chemistry of apatites. *Acta Crystallogr., Sect. B: Struct. Sci.* **2003**, *59* (1), 1–16.
- (45) Lim, S.; Baikie, T.; Pramana, S. S.; Smith, R.; White, T. J. Apatite metaprism twist angle (φ) as a tool for crystallochemical diagnosis. *J. Solid State Chem.* **2011**, *184* (11), 2978–2986.
- (46) Samanta, S. K.; Das, P.; Sengupta, A.; Acharya, R. Optimization of external (in air) particle induced gamma-ray emission (PIGE) methodology for rapid, non-destructive, and simultaneous quantification of fluorine, sodium, and phosphorus in nuclear waste immobilization matrices. *RSC Adv.* **2022**, *12* (50), 32684–32692.
- (47) Klee, W. The vibrational spectra of the phosphate ions in fluorapatite. *Zeitschrift für Kristallographie-Crystalline Materials* **1970**, *131* (1–6), 95–102.
- (48) Baddiel, C.; Berry, E. Spectra structure correlations in hydroxy and fluorapatite. *Spectrochim. Acta* **1966**, *22* (8), 1407–1416.
- (49) Das, P.; Vats, B. G.; Mohapatra, M.; Rai, A. K.; Samui, P.; Shafeeq, M.; Parida, S. Effect of strontium loading on the structural and thermodynamic properties of Ca_{10-x}Sr_x(PO₄)₆F₂ (x = 2, 4, 6, 8) solid solutions for radioactive waste immobilization. *J. Solid State Chem.* **2023**, *324*, No. 124101.
- (50) Dorogova, M.; Navrotsky, A.; Boatner, L. A. Enthalpies of formation of rare earth orthovanadates, REVO₄. *J. Solid State Chem.* **2007**, *180* (3), 847–851.
- (51) Helean, K.; Navrotsky, A. Oxide melt solution calorimetry of rare earth oxides. *J. Therm. Anal. Calorim.* **2002**, *69*, 751–771.
- (52) Navrotsky, A. Progress and new directions in calorimetry: A 2014 perspective. *J. Am. Ceram. Soc.* **2014**, *97* (11), 3349–3359.
- (53) Zhang, Y.; Navrotsky, A. Thermochemistry of rare-earth aluminates and aluminosilicate glasses. *Journal of non-crystalline solids* **2004**, *341* (1–3), 141–151.
- (54) Barin, I.; Platzki, G. *Thermochemical data of pure substances*; Wiley Online Library: 1989.

- (55) Kubaschewski, O.; Alcock, C. B.; Spencer, P. *Materials thermochemistry*; 1993.
- (56) Hosseini, S. M.; Drouet, C.; Al-Kattan, A.; Navrotsky, A. Energetics of lanthanide-doped calcium phosphate apatite. *Am. Mineral.* **2014**, *99* (11–12), 2320–2327.
- (57) Ranganathan, S. Alloyed pleasures: Multimetallc cocktails. *Curr. Sci.* **2003**, *85* (5), 1404–1406.
- (58) Utsunomiya, S.; Yudintsev, S.; Wang, L.; Ewing, R. Ion-beam and electron-beam irradiation of synthetic britholite. *J. Nucl. Mater.* **2003**, *322* (2–3), 180–188.
- (59) Meldrum, A.; Wang, L.; Ewing, R. Electron-irradiation-induced phase segregation in crystalline and amorphous apatite: A TEM study. *Am. Mineral.* **1997**, *82* (9–10), 858–869.
- (60) Váczi, T.; Nasdala, L. Electron-beam-induced annealing of natural zircon: a Raman spectroscopic study. *Physics and Chemistry of Minerals* **2017**, *44*, 389–401.
- (61) Rocca, F.; Kuzmin, A.; Purans, J.; Mariotto, G. X-ray-absorption spectroscopy of a Nd 3+-exchanged β'' -alumina crystal. *Phys. Rev. B* **1994**, *50* (10), 6662.
- (62) Xu, L.; Niu, M.; Wang, H.; Su, L.; Gao, H.; Zhuang, L. Response of structure and mechanical properties of high entropy pyrochlore to heavy ion irradiation. *Journal of the European Ceramic Society* **2022**, *42* (14), 6624–6632.
- (63) Sickafus, K.; Minervini, L.; Grimes, R.; Valdez, J.; Ishimaru, M.; Li, F.; McClellan, K.; Hartmann, T. Radiation tolerance of complex oxides. *Science* **2000**, *289* (5480), 748–751.
- (64) Wang, F.; Yan, X.; Wang, T.; Wu, Y.; Shao, L.; Nastasi, M.; Lu, Y.; Cui, B. Irradiation damage in (Zr_{0.25}Ta_{0.25}Nb_{0.25}Ti_{0.25})C high-entropy carbide ceramics. *Acta Mater.* **2020**, *195*, 739–749.
- (65) Lu, C.; Niu, L.; Chen, N.; Jin, K.; Yang, T.; Xiu, P.; Zhang, Y.; Gao, F.; Bei, H.; Shi, S.; et al. Enhancing radiation tolerance by controlling defect mobility and migration pathways in multi-component single-phase alloys. *Nat. Commun.* **2016**, *7* (1), 13564.
- (66) Ravel, B.; Newville, M. ATHENA, ARTEMIS, HEPHAESTUS: data analysis for X-ray absorption spectroscopy using IFEFFIT. *Journal of synchrotron radiation* **2005**, *12* (4), 537–541.